

ABSTRACT

Title of Document: MANIFOLD MICRO-CHANNEL COOLING
 OF PHOTOVOLTAIC CELLS FOR HIGH
 EFFICIENCY SOLAR ENERGY
 CONVERSION SYSTEMS

Elnaz Kermani, Master of Science 2008

Directed By: Professor Michael Ohadi, Mechanical
 Engineering

Several works have been published on concentration of solar radiation by mirrors or lenses onto smaller sized solar panels, which reduce cost and increase conversion efficiency at higher concentration ratio. One of the challenges is active and uniform cooling of high heat flux solar arrays, because conversion efficiency is dependent on device temperatures and drops with increasing temperature.

This research is targeted at cooling small, high concentrated solar cells. Benefits of manifold microchannel are attractive for cooling of electronic devices but have not been studied for cooling of high concentrated solar cells which is the target of this research, where the microchannel can be microfabricated and etched on the backside of the silicon solar cell to form a sealed heat sink with the manifold fabricated in the silicon substrate. This design not only minimizes the pressure drop, but also maximizes the heat transfer and provides uniform temperature across the device.

MANIFOLD MICRO-CHANNEL COOLING OF PHOTOVOLTAIC CELLS FOR
HIGH EFFICIENCY SOLAR ENERGY CONVERSION SYSTEMS

By

Elnaz Kermani

Thesis submitted to the Faculty of the Graduate School of the
University of Maryland, College Park, in partial fulfillment
of the requirements for the degree of
Master of Science
2008

Advisory Committee:
Professor Michael Ohadi, Chair
Professor Reinhard Radermacher
Professor Gary A. Pertmer

© Copyright by
Elnaz Kermani
2008

Dedication

This work is dedicated to my family whose encouragement helped me to complete it and who have supported me.

Acknowledgements

First and foremost I would like to thank Dr. Serguei Dessiatoun whom I am indebted for his help in conducting this research and for his constructive guidance and advices during my study. I would also like to thank my advisor Dr. Michael Ohadi and Dr.

Amir Shooshtari for their support during my course of study.

During the course of my research I had an opportunity to work with Thomas Loughran, Jonathan Hummel, and John Abrahams in Fabrication Laboratory of University of Maryland whom I wish to express my sincere gratitude.

Also I would like to thank Center for Nanophysics and Advanced Materials in University of Maryland for providing support for my research.

Furthermore I would like to thank my colleagues at the Smart and Small Thermal System Laboratory for providing constructive and fun environment in the laboratory especially Parisa Foroughi, Ebrahim Alhajri, Mohammad Alshahi, and Edvin Cetegen.

Table of Contents

Dedication	ii
Acknowledgements	iii
List of Tables	vii
List of Figures	viii
Chapter 1: Introduction	1
1.1 Background and Problem Statement	1
1.2 Motivation and Objectives	3
Chapter 2: Literature Review	5
2.1 Introduction to Concentrated Solar Cell	5
2.1.1 High and Non-Uniform Illumination	6
2.1.2 Non-Uniform Temperature	7
2.1.3 Temperature and Concentration Dependency of the Solar Cell Parameters	8
2.1.4 Hybrid PV-Thermal System	11
2.2 Introduction to Microchannel Cooling Studies	13
2.2.1 Manifold Microchannel Studies	14
2.3 Summary	18
3.1 Introduction	20
3.2 Design Strategy	20
3.3 Microchannel Design	22
3.4 Manifold Design	23
3.5 Heater Design	25

3.6 Package Size	26
3.7 Numerical Analysis.....	27
3.8 Summary	37
Chapter 4: Fabrication Process	38
4.1 Introduction.....	38
4.2 Photolithography to Generate the Pattern	39
4.3 Etching the Manifold on the Silicon Wafer using DRIE	40
4.4 Etching the Inlet and Outlet holes in the Silicon wafer Using DRIE	42
4.5 Etching Microchannel in the Silicon Wafer Using DRIE.....	43
4.6 Scan Electron Microscopy (SEM)	44
4.7 Bonding of Microchannel Wafer and Manifold Wafer:	46
4.8 Microfabrication of Heater	50
4.9 Packaging Procedure.....	54
4.10 Wirebonding	55
4.11 Summary	57
Chapter 5: Experimental Setup and Results	58
5.1 Introduction.....	58
5.2 Instruments and Measurement Devices	58
5.2.1 Calibration of Thermocouples	60
5.3 Test Module	61
5.4 Experimental Procedure.....	62
5.5 Experimental Results	63
5.5.1 First Sample	63

5.5.2 Second sample	67
5.6 Comparison Between the Results of the First and Second Sample	71
5.7 Summary	79
Chapter 6: Conclusion and Recommendation for Future Work	80
6.1 Introduction.....	80
6.2 Conclusions.....	80
6.3 Recommendations for Future Work.....	83
6.4 Summary	84
Bibliography	85

List of Tables

Table 1: Geometrical dimension of the microchannels.	22
Table 2: Geometrical dimension of the manifold.	23
Table3: Effect of change in computational element geometry on heat transfer at constant heat flux of 100 W/cm ²	36
Table 4: Sequence of microfabrication procedure.	53
Table 5: Geometrical dimension of the samples tested.	61

List of Figures

Figure 1: Solar cell efficiency versus concentration for a single cell based on theory.	
.....	10
Figure 2: Schematic of manifold heat sink adopted from [35]	14
Figure 3: Schematic design of the cooling device with mircochannels and flow distributor.....	22
Figure 4: CAD drawing of the mask used for patterning the microchannel.....	23
Figure 5: Schematic drawing of the manifold.....	24
Figure 6: CAD drawing of the mask used for patterning the manifold.	25
Figure 7: CAD drawing of the mask used for patterning inlet and outlet holes.	25
Figure 8: Schematic drawing of the heater.	26
Figure 9: CAD drawing of the mask used for patterning the heater.....	26
Figure 10: CAD drawing of the housing.....	27
Figure 11: Computational domain.	28
Figure 12: Velocity distribution in the fluid domain for the first design with channel width of.....	30
Figure 13: Temperature distribution in fluid domain for first design with channel width of 20 μm and equal inlet and outlet.	30
Figure 14: Velocity distribution in the fluid domain for the first design with channel width of 20 μm and outlet twice the inlet.	31
Figure 15: Temperature distribution in fluid domain for the first design with channel width of 20 μm and outlet twice the inlet.	32

Figure 16: Velocity distribution in the fluid domain for the first design with channel width of 80 μm and inlet equals outlet.	33
Figure 17: Temperature distribution in fluid domain for first design with channel width of 80 μm and inlet equals the outlet.....	33
Figure 18: Velocity distribution in the fluid domain for first design with channel width of 80 μm and outlet twice the inlet.	34
Figure 19: Temperature distribution in fluid domain for first design with channel width of 80 μm and outlet twice the inlet.	35
Figure 20: Picture of the manifold wafer after DRIE.	41
Figure 21: Picture of the back side of manifold wafer after inlet and outlet holes etched.	43
Figure 22: Picture of a completed manifold wafer.	43
Figure 23: Picture of the microchannel silicon wafer after DRIE.	44
Figure 24: SEM image of the 20 μm width microchannel.	45
Figure 25: SEM image of the 40 μm width microchannel.	45
Figure 26: SEM image of the manifold wall.	46
Figure 27: SEM image of the manifold corner.	46
Figure 28: Image of the sample wafer bonded in 800 $^{\circ}\text{C}$	48
Figure 29: Image of a wafer bonded in 600 $^{\circ}\text{C}$	48
Figure 30: Two silicon wafer with deposited metal stack.	49
Figure 31: X-ray image of bonded wafers.	49
Figure 32: Lift off Sequence with positive photoresist [27].	50
Figure 33: Image of a sample fabricated heater.	52

Figure 34: G10 housing with inlet and outlet connections.	54
Figure 35: Packaged sample with thermocouples and electrical connections.	56
Figure 36: Schematic of test setup.	59
Figure 37: Picture of test setup.	60
Figure 38: Thermocouple Calibration Curve.	61
Figure 39: Picture of test module.	62
Figure 40: Variation of pressure drop versus flow rate for first sample with 67 μ m hydraulic diameter.	64
Figure 41: Variation of heat transfer coefficient versus flow rate for sample with 67 μ m hydraulic diameter.	65
Figure 42: Variation of water temperature difference versus input power for sample with 67 μ m hydraulic diameter.	66
Figure 43: Variation of heater surface temperature difference versus input power for sample with 67 μ m hydraulic diameter.	67
Figure 44: Variation of pressure drop versus flow rate for sample with 36 μ m hydraulic diameter.	68
Figure 45: Variation of heat transfer coefficient versus flow rate for sample with 36 μ m hydraulic diameter.	69
Figure 46: Variation of water temperature difference versus input power for sample with 36 μ m hydraulic diameter.	70
Figure 47: Variation of heater surface temperature difference versus input power for second sample.	71
Figure 48: Comparison of pressure drop between first and second sample.	72

Figure 49: Pressure drop in the manifold for the two test cases.	74
Figure 50: Total and manifold pressure drop for sample with hydraulic diameter of 67 μm	75
Figure 51: Total and manifold pressure drop for sample with hydraulic diameter of 36 μm	76
Figure 52: Variation of Nusselt number versus Reynolds number for first and second sample.	77
Figure 53: Variation of Nusselt versus X^+ for two sample cooler.	78
Figure 54: Comparison of Nusselt number versus X^+ number of the experiment against Jiang et al. [26] correlation.	79

Chapter 1: Introduction

1.1 Background and Problem Statement

The abundance of solar energy in the world provides significant opportunity for development of eco-friendly power generation technologies essential in the modern world. Among several techniques enabling the use of solar energy, PV systems exhibit significant potential for economic and eco-friendly process for power generation industry. After five decades of research and development, photovoltaic energy production is growing exponentially across global markets. Northern Europe and Japan currently lead in the research and commercialization of PV technology [1]. Solar panels on the facades and roofs of commercial and residential buildings are common pictures in these countries, where solar energy is used in every aspect of utilities, including heating, cooling and lighting needs. Most of those countries have climates with high cloudiness and low intensity direct sunlight, limiting the energy conversion effect. The static PV arrays that work well with dispersed sun light have already been developed. These cells are used in the static arrays and are simple silicon-based cells with poor conversion efficiency.

Progress has been made on decreasing the cost and consumption of solar array material by using thin film PV cells. Daytime tracking of the sun by sensor-enabled drives offers significant benefit in increasing solar array effectiveness.

By the 1973 oil crisis, research on concentrating PV systems began in earliest 1975 [1]. Several decades of research have produced significant knowledge and innovations in design of economically viable, silicon-based photovoltaic (PV) panels and mirrors for concentration of solar radiation and its conversion to electric power. In a research by Swanson et al. [1] it is indicated that from 1975 through 1992, the total funds expended world wide on trying to develop concentrating PV was probably over \$40 million.

Several works have been published on the concentration of solar radiation by parabolic mirrors and lens structures onto smaller sized solar panels, which greatly reduce the cost and increase conversion efficiency by increasing specific power. The US Department of Energy has recently reported exceeding 40% efficiency level with concentrated arrays compared to 8.5% for static arrays. The efficiency of the array increases with the level of concentration if array temperature is kept at a low constant value. The same low array cost compared to the total system cost will allow updating to current technology. The radiation concentration up to 84,000 times is theoretically possible [2] but currently just 400 to 500 times is feasible due to high heat dissipation requirement on the PV concentrator arrays.

One of the outstanding challenges in this field is the active and uniform cooling of these large-area, high heat flux solar concentrator arrays, because the conversion efficiency is heavily dependent on device temperatures and drops significantly with an increase in temperature. If an appropriate cooling technique is possible, these solar

panels will become more effective and commercially viable, which could pave the way for a rapid transition of the current power generation industry towards eco-friendly alternatives for local use, increasing currently available export resources and also creating a base for future energy export technologies.

1.2 Motivation and Objectives

The above section explained why new methods for concentrated solar cell cooling will be needed in the near future. This project is conducted to investigate the performance of a novel cooling method and develop functionality of that method in cooling of high heat flux solar cells for active and uniform surface cooling. This new method is called manifold microchannel cooling and will be described in chapter two. It is believed that this technology has the capability to solve the problem of cooling the concentrated solar cell and more importantly pave the way to bring that technology in to market.

This research has two principal objectives. First to design and micro fabricate both the manifold and microchannel out of silicon and package the system, second to study the performance of the proposed system to investigate the applicability of the technology for cooling of concentrated solar cells.

The first objective will be met by series of micro fabrication processes to build the designed system and package it as will be discussed in chapter three for designing strategies, and chapter four for fabrication. The second objective is met by developing

an experimental setup to investigate the performance of the cooling device and its ability to remove a given amount of heat from the surface and keeping the surface at uniform temperature as the experimental procedure and results will be discussed in chapter five. Finally chapter six will discuss the conclusion and recommendation for future works on manifold microchannel and its application for cooling of high heat flux concentrated solar cells.

Chapter 2: Literature Review

2.1 Introduction to Concentrated Solar Cell

Solar energy is perhaps one of the world's most valuable sources of energy and has the potential to produce a significant portion of the world's energy usage if appropriate technologies for its efficient collection and utilization are developed.

Solar thermal and photovoltaic (PV) systems are the major solar energy technologies. While photovoltaic cells utilize only a small fraction of solar radiation, from 15 % for commercial usage to 40% for research lab cells [1], concentrating systems can focus sunlight onto solar cells for higher conversion to electricity with lower costs.

Concentrator PVs seem to have the potential to be the least expensive of all PV technologies [1].

Despite the fact that maximum solar flux concentration of up to 84000 has been reached experimentally [2], there are limited studies on the development of medium- to high-concentration collectors due to challenging issues concerning the design and performance of the PV concentrating systems. One of the most important challenges in high-concentration PV collectors is designing a system to achieve high fluxes of solar radiation with uniform flux distribution. High and non-uniform heat flux due to concentrated solar radiation affects the temperature distribution of the solar cell, resulting in a change of solar cell parameters, mainly the conversion efficiency [10]. It is well known that the efficiency of PV cells decreases dramatically with an

increase in cell temperature, which explains the need for an effective cooling method for concentrating systems. The solar cell cooling method becomes a limiting factor in the development of highly concentrated modules. One of the proposed ways to cool the concentrated PV modules is to use the hybrid systems to recover part of the waste heat and use it for other practical applications. This system maintains high electrical efficiency, and excess heat can be harnessed by combining both the thermal and photovoltaic system in a hybrid PV/thermal system so that the combined efficiency increases.

The first part of this chapter provides a review of the phenomena occurring in concentrated PV systems, such as non-uniform illumination resulting in non-uniform temperature and the effect of non-uniformity on solar cell parameters. And in the second part of this chapter manifold microchannel cooling system will be reviewed.

2.1.1 High and Non-Uniform Illumination

One of the major concerns in designing a concentration system for PV modules is achieving an acceptable uniform radiation flux distribution on the PV cells. This is the major challenge reported by many scientists for medium to high concentration level modules [4], [5], and [6]; however, only limited investigations on this issue have been reported in literature.

Luque et al. [34] studied the effect of non uniformity on the EUCLIDES solar collector prototype [17], consisting of a linear photovoltaic concentrator with mirror

optics. Distribution of the illumination on the PV cell was collected by a CCD camera. They concluded inhomogeneous irradiance distribution occurs on the cell, which will result in non-uniform temperature distribution in the cell.

Coventry et al. [7] investigated the flux intensity for the domestic combined heat and power solar system (CHAPS), which utilizes a concentrating parabolic trough system. They demonstrated that, while the overall concentration ratio for the CHAPS system was 30X, flux density peaks at upward of 100 suns in the center of the cell.

The non-uniform light illumination across a cell has major effects on solar cell temperature distribution and influences the distribution of current and voltage in the solar cells. It also needs modifications in the IV curves. Moreover, for solar cells connected in series to have same current, since current is linearly proportional to incident light, the current in the string of identical solar cells will be limited by the cell with the least illumination [10].

2.1.2 Non-Uniform Temperature

One of the major effects of non-uniform illumination is local heating in solar cells, which will reduce the efficiency of the solar cell. Luque et al. [4] has developed an analytical method to predict the temperature distribution on a PV cell. They assumed that the surface is isothermal and the light is radiated homogeneously on the segment. Their results confirmed that severe temperature non-homogeneities occur in the cell,

and hence the strong local hot spot produced by the non-uniform illumination could cause a temperature drop of 36.4°C .

In another study by Coventry et al. [7], temperature distribution for the domestic CHAPS system was simulated using commercial STRAND7 (finite element analysis base software [36]) software under typical conditions of light breeze, turbulent fluid flow, and water temperature at 55°C in the receiver. Temperature profile across the solar cell showed a temperature difference of up to 14°C between the middle of the cell and the edges.

Non-uniform illumination caused by the type of concentrator, tracking error, receiver support post shading, mirror imperfection, gaps between the mirrors, and the assembly of the module has a significant effect on temperature distribution in the solar cells and must be studied in particular cases. These non-uniformities have a significant impact on different cell parameters, such as open circuit voltage, short circuit current and overall electrical performance, which are the subject of next section.

2.1.3 Temperature and Concentration Dependency of the Solar Cell Parameters

It is well known that by increasing the mean solar cell temperature, the efficiency decreases [3], [8], and [9]. The main reason for this decrease is the drop in the open circuit voltage and fill factor. The reduction in solar cell efficiency is on the order of $0.35\% / ^{\circ}\text{C}$ [10].

Meneses-Rodriguez et al. [11] have studied the PV solar cell performance at high temperature theoretically. They confirmed that the open-circuit voltage and fill factor decrease with temperature and concluded that the main reason for the decrease in efficiency is the decrease in the open circuit voltage and fill factor. They also studied the effect of light flux concentration on cell parameters at 300 °K and concluded that the increase in short circuit current with concentration level is much steeper than the increase in open-circuit voltage. Efficiency also increases with concentration level. They concluded that for effective performance, the proper combination of solar concentration and temperature must be chosen.

Sun incident irradiance during a day can be written as following:

$$I_{rad}(t) = 1000 \sin\left(\frac{\pi}{16}(t - 6)\right)$$

Where t is the hour of a day and is between 6 and 18. The variation of solar cell efficiency with temperature is calculated as [3]:

$$\eta = \eta_{ref} (1 - \beta(T - T_{ref}))$$

Where β is cell reference parameter varying between 0.004 and 0.006 1/°C and η_{ref}, T_{ref} are reference efficiency and temperature. For a simple assumption of a 1000 concentration sun on a solar cell with reference efficiency of 25% and no convection from front and back surfaces, maximum heat should be removed from the solar cell to keep the cell temperature below 110 °C, is approximately 75 W/cm². Maximum cell temperature occurs at 2 pm when the sun irradiance is at its maximum level.

Markvart [9] suggested a logarithmic relationship for efficiency of cells under concentration based on short-circuit current and open-circuit voltage as following:

$$\eta(X) = \frac{V_{oc}(X)I_{sc}(X)FF}{G(X)} = \eta(1)[1 + \frac{kT}{qV_{oc}(1)} \ln(X)]$$

Where q is the magnitude of electron charge given as $1.602 \times 10^{-19} \text{ C}$, T is the temperature, and k is the Boltzmann constant $1.38 \times 10^{-23} \text{ J/K}$, and $\eta(1)$, $V_{oc}(1)$ are the efficiency and open-circuit voltage of solar cells without concentration. Based on this equation, a solar cell efficiency graph versus concentration is plotted in Figure 1 for assumed input parameters of $V_{oc}=0.6 \text{ V}$, $I_{sc}= 0.05 \text{ A}$, and $KT/q= 0.026 \text{ V}$.

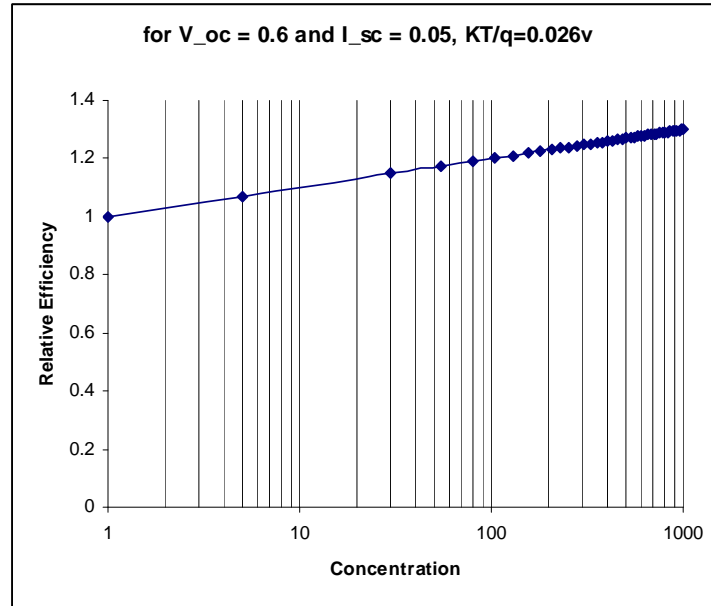


Figure 1: Solar cell efficiency versus concentration for a single cell based on Markvart [9].

The effects of temperature, variations in the levels of concentration, and non-uniform illumination on the solar cell parameters have been studied. It is clear from these

studies that efficiency decreases with the increase in temperature and short-circuit current slightly increases with temperature; however, the exact value is not reported.

Furthermore, all the research shows that efficiency, open-circuit voltage, and short-circuit current increase with concentration ratio; however, there seems to be no agreement on their values [10], [11], [12], and [13]. The effect of non-uniform illumination is less studied; and, this area needs further investigation especially in terms of the effect of non-uniform temperature due to non-uniform illumination on cell parameters. These studies prove that the need for effective and non-uniform cooling is obvious especially for cases of high concentration levels in which cell efficiency decreases severely due to high cell temperature.

2.1.4 Hybrid PV-Thermal System

One of the most efficient ways to take advantage of hot solar cell temperatures under concentration is to combine solar cells in a hybrid system and co-generate heat and electricity. Using a concentrated hybrid system will increase the total efficiency of the system and lead to a reduction of PV cell required area. [10], [15] [16]

Brogren et al. [14] conducted several studies on a water-cooled hybrid system with low-concentration aluminum compound parabolic concentrator (CPC) with geometric concentration of 4X. Their system consists of three rows of CPCs, and in each row there were four 12-cell string modules cooled by water circulating in a cooling fin bonded on the back of the modules. The PV cells used in this prototype are monocrystalline with total cell area of 1.5 m^2 and a total glaze collector area of 7.2 m^2 .

Complete information about the experimental setup, system description, and material properties can be found in [14]. Electrical and thermal performance of the PV-thermal hybrid on a clear day was studied. The maximum electric power and the recovered heat were about 330 W and 2300 W, respectively, at low temperature per square meter cell area. In comparison, a conventional plane PV module with the same cell area and without concentration would have delivered 225 W of electric power; therefore, one can conclude that in hybrid system the total power output is increased.

Non-uniform distribution of solar light on the cell surface results in an uneven current distribution, which causes a reduction in electric output due to resistive losses and voltage drop at high irradiation, and thus the efficiency decreases.

Coventry et al. [7] investigated thermal and electrical performance of a CHAPS utilizing parabolic mirrors to concentrate light combined with photovoltaic (PV) cells and thermal energy absorption to produce electricity and hot water. Their prototype system consisted of a 25X concentrator with a two-axis tracking system and two individual mirrors each 1.6 m long and 1.2 m wide, with 0.2 m height. For detailed information on the experimental set-up refer to [7]. As the operating temperature increases in the afternoon at around 2:00, this causes higher convective and radiative losses, and the thermal efficiency decreases from about 50% to 40%.

Coventry [10] studied the performance of a long CHAPS with parabolic trough PV-thermal collector. The major components, such as the receiver, mirrors, and solar cells are essentially the same as the domestic system [7]. The collectors are made of

10 mirrors, each 1.6 m wide, and 1.5 m long parabolic trough mirrors, and receiver modules, which are connected end-to-end to form a row. The mirror receiver and solar cell widths are 1.5, 0.08, and 0.04 m, which yield a geometric concentration of 37X, excluding the shading due to the receiver. He concluded that under typical operating conditions the CHAPS collector has a thermal efficiency of 58% and electrical efficiency of 11%, and therefore a combined efficiency of 69%.

2.2 Introduction to Microchannel Cooling Studies

As described in the previous section and also in Chapter One, there is a great need for active and uniform cooling methods for high concentrated solar cells. Since the 1980s, when Tuckerman and Pease [18] first proposed the use of microchannel heat sink in cooling integrated circuits, many research studies have been done on the performance and mechanism of microchannel cooling. Traditional microchannel heat sinks have one inlet and one outlet channel located at the end of the chip length. Although standard microchannel heat sinks provide high cooling capacity, they could have two major drawbacks. Due to their narrow channel width, they have a high pressure drop, and there is a significant temperature difference between the inlet and outlet fluid along the channel length. However, with innovative manifold and optimum micro channel geometric configuration such drawbacks could be minimized.

The innovative design of the microchannel heat sink proposed in this study includes a manifold microchannel, as depicted in Figure 2, and features many inlet and outlet channels, alternating at a periodic distance along the length of the channel. By this

method pressure drop and temperature difference will reduce. This section provides an overview of the kind of work that has been done in this field that is relevant to the present work.

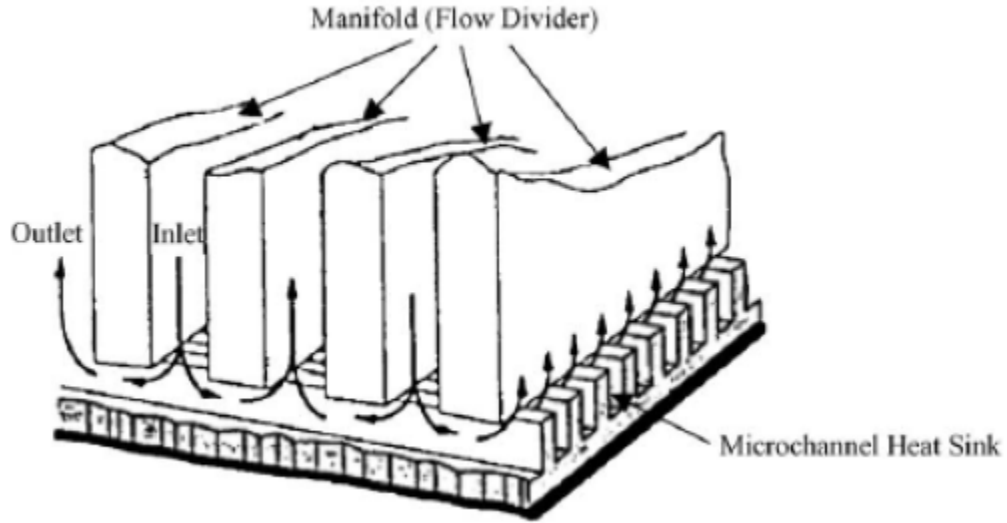


Figure 2: Schematic of manifold heat sink adopted from [35]

2.2.1 Manifold Microchannel Studies

One of the first studies in manifold microchannels was done by Harpole et al. [19] in 1991. They developed a 2D numerical modeling of multi-dimensional flow to optimize the design parameters. In their modeling they assumed single-phase laminar flow, and explained that the micro-manifold can reduce pressure drop by several orders of magnitude because the manifold subdivide the flow so that flow paths through microchannels are short and the local flow velocity is low.

Their optimization demonstrated that for the case of 1 kW/cm^2 heat flux, with top surface at 25°C , the water flow rate should be 50 cc/s per cm^2 of surface area. The center-to-center manifold spacing should be $333 \text{ }\mu\text{m}$ (30 channel /cm). The fin height

should be about 167 μm and distribution manifold channel widths should be about 200 μm . The microchannel should be between 7 μm and 14 μm wide, while the ratio of fin thickness to microchannel thickness should be between 0.5 to 1.

Copeland et al. [20] used a 3D finite element model (Fluent, Version 4.3.1) of an isothermal single manifold microchannel to simulate fluid flow and heat transfer. They assumed laminar flow, constant properties, uniform wall temperature, and uniform inlet velocity. The fluorocarbon liquid FX-3250 was used as the coolant. Uniform grid spacing was used, with $80 \times 16 \times 10$ fluid element and 1000 μm pitch manifold.

Their study demonstrated that a region of high heat transfer exists near the inlet, at the base of microchannel below the inlet and at the top of the microchannel near the exit.

Later, Ryu et al. [21] developed a 3D analysis procedure for the thermal performance of a manifold microchannel heat sink. The equations were solved by a SIMPLE-type finite volume method in which the optimal geometric shape was traced by a steepest descent technique. They simulated a square horizontal surface heat sink with 1 cm \times 1 cm dimension. Water was the coolant, silicon was the heat sink material, and copper was the divider material.

They concluded that thermal resistance is inversely proportional to the volume flow rate in a log-log scale. Also, they explained that the cooling is most effective in the channel entrance region directly under the inlet manifold. Their results also

demonstrate that two different flow regimes exist based on the number of channels per centimeter. For the number of channels per cm less than 120, the channel aspect ratio is low (2-5), and the inlet to outlet width ratio is (<2), but for the number of channels per centimeter greater than 200, the channel aspect ratio becomes high (>10) and so does the inlet to outlet width ratio (>2.5).

Xu et al. [22] demonstrated a new microchannel heat sink comprised of parallel longitudinal microchannels and several transverse microchannels to separate the whole flow length to several zones. The whole length of the parallel microchannels in longitudinal direction was 21.45 mm, and the total width covering the ten triangular microchannels was 4.35 mm with a hydraulic diameter of 155 μm . The microchannels were made of silicon and thin film platinum deposited with chemical vapor deposition technique, which provided uniform heat flux.

In their experiment they had ten parallel longitudinal triangular microchannels and five transverse trapezoid microchannels. The local chip temperature and Nusselt number were obtained using a high resolution infrared radiator imaging system. Their results proved that by separating the whole flow length into several independent zones, thermal developing flow occurs in each zone and the overall heat transfer is enhanced. Their experiment demonstrated that the chip temperature and Nusselt number for their heat sink display cyclic behavior along the flow length, supporting the concept of periodic redeveloping of thermal boundary layer. Their Nusselt number for new heat sink increased 26.4% compared with the conventional one.

Xu et al. [22] also discussed the pressure drop for the new heat sink, and in a comparison with a conventional micro channel heat sink demonstrated that pressure drop decreased 27% in the new design. Very small flow velocity and shortened flow length were the main reasons for decrease in pressure drop in this design.

In another study by Wang et al. [23] parallel longitudinal microchannels etched in silicon substrate and transverse microchannels electroplated on a copper heat spreader were studied. The copper heat spreader was eutectic-bonded to silicon substrate through a bonding layer to create a sealed microchannel system. A nickel heater, as a heat source simulative, was integrated in the copper heat spreader, and de-ionized water was used as the working fluid. They measured the steady state temperature distribution of the bottom surface of the silicon substrate with a high-accuracy infrared radiator imaging system.

They obtained a uniform temperature distribution through the heating area where repeating of redeveloping of thermal boundary layer occurs for transverse channel. They concluded that transverse microchannels not only repeat the occurrence of periodic thermal boundary layer but also increase the heat transfer area compared with conventional channels, and these benefits are attractive for the cooling of high heat flux electronic devices.

In another paper Wang et al. [24] simulated the same transverse microchannel and explained that maximum heat flux input of the new microchannel heat sink was 75% more than that of conventional ones. He obtained an average wall heat transfer coefficient of about $3186.8 \text{ W/m}^2\text{K}$ with a flow rate of 6.7 ml/min and 20300 W/m^2 heat flux.

A similar study was conducted by Everhart et al. [25] to fabricate and test manifold and microchannel cooler for single-phase forced convection flow. They fabricated a $25 \text{ mm} \times 5 \text{ mm} \times 1.5 \text{ mm}$ -thick cooler to cool a $4 \text{ mm} \times 4 \text{ mm} \times 0.4 \text{ mm}$ -thick SiC diode. They used a 1 mm -thick silicon wafer to create both the microchannel and the manifold channels, which manifolds were $200 \text{ }\mu\text{m}$ wide and $800 \text{ }\mu\text{m}$ deep. The microchannels were $20 \text{ }\mu\text{m}$ wide and $200 \text{ }\mu\text{m}$ deep. The SiC diode was bonded directly on to the cooler using a gold tin eutectic bond.

Their experiment demonstrated that the cooler can achieve a flow rate range from 1 to 2.5 mL/s with pressure drop between 5 and 20 psi linearly. They also obtained a $45 \text{ }^\circ\text{C}$ diode temperature increase and a $7.9 \text{ }^\circ\text{C}$ temperature increase in fluid temperature for 100 W power input.

2.3 Summary

The first section of this chapter covered a brief introduction to concentrated solar cells and discussed common phenomena that occur in concentrated solar cell technology. It also briefly introduced one of the most important limitation factors in

the development of the solar cell thermal conversion technology (the difficulty of achieving uniform heat fluxes) and discussed the importance of the active and uniform cooling technique for concentrated solar cells to become commercially more viable.

The second section covered some advanced heat sink techniques in relation to the use of the manifold microchannel technique for cooling of concentrated solar cells.

The work presented in this thesis utilizes this advanced technology for cooling of concentrated solar cells and the evaluation of the cooling performance. In the following chapters the details of work conducted for this thesis are described.

Chapter 3: Design Procedure and Numerical Modeling

3.1 Introduction

The previous chapter demonstrated that concentrated solar cells need effective and uniform cooling to operate under the desired efficiency conditions. Based on the requirements discussed in the previous chapter for concentrated solar cells, single-phase microchannel cooling, which is capable of dissipating high heat flux and has low volume and weight, was selected for this research. Single-phase liquid cooling with water in micro channels is one of the most effective cooling technologies to produce high heat transfer coefficients [34]. However this technology has a major disadvantage of high pressure drops due to very narrow channels. To overcome this problem, a manifold (flow distributor) was designed which distributes the flow in the channel such that there is minimum pressure drop. In the following chapter the cooling device dimensions and characteristics will be discussed and preliminary results of numerical modeling presented.

3.2 Design Strategy

In this study the microchannels were made of silicon, which means in an actual design there will be no contact resistance between the solar cell and the cooler, since the solar cells are also made of silicon. Moreover, the flow distributor was also fabricated from silicon to match the CTE and was bonded to the microchannel wafer.

The strategy in dimension selection was to fabricate two different microchannel designs and two different manifold designs on 4" diameter silicon wafers to yield four different combinations. Since this research was designed to simulate the conditions of concentrated solar cell cooling, the size of the microchannels and the flow distributor was assumed to be $1\text{ cm} \times 1\text{ cm}$. The microchannels were made of 0.5 mm-thick silicon wafers, and the flow distributors were made out of 1 mm thickness silicon wafers. It should be mentioned that because of the microfabrication facility available at the University of Maryland, a 4" diameter silicon wafer is selected. The microchannels and manifold wafers were bonded together to form the cooler.

Later a gold resistance, which will represent the solar cell heat load, was fabricated on the backside of the microchannel silicon wafer to represent heated surface. The area of the heater should be $1\text{ cm} \times 1\text{ cm}$. The last step was to design a packaging box for the cooler and to make electrical connections.

In the manifold microchannel, a flow distributor, which is the manifold in this study, was placed on top of the micro-structured surface to guide the cold flow into the microchannel and the hot flow out of the channel. The liquid heats as it passes a short distance in the microchannel, and then the manifold guide it to the outlet. Therefore, the net effect can be represented as hundreds of microchannels operating in parallel with very short lengths, which will provide very low pressure drop. In Figure 3 a schematic of the designed manifold microchannel is presented.

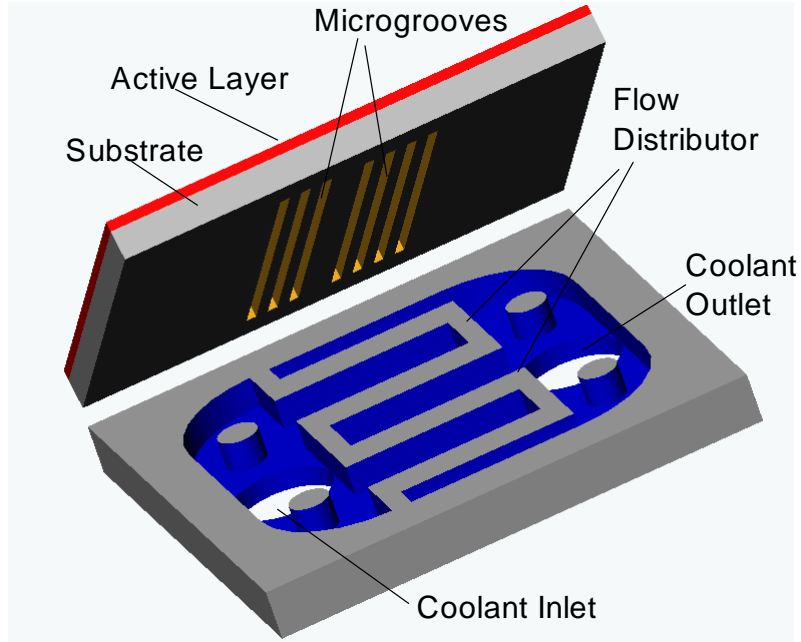


Figure 3: Schematic design of the cooling device with microchannels and flow distributor.

3.3 Microchannel Design

The microchannels were designed to have two different widths but the same depth to have different aspect ratios. All the microchannels had 200 μm depths, and therefore a 0.5 mm thickness silicon wafer was selected for microfabrication. Also, the channel thickness was equal to the wall thickness. The dimensions of the microchannels are listed in Table 1.

Table 1: Geometrical dimension of the microchannels.

Hydraulic Diameter (μm)	36	67
Channel Width (μm)	20	40
Channel Depth (μm)	200	200
Channel Aspect Ratio	10	5
# Channel/ cm	250	125
Channel Length (mm)	400	400

The first step in fabrication of the designed microchannel was drawing a mask to transfer the microchannel plan to the silicon wafer. The fabrication mask drawn in Auto CAD for the fabrication of the microchannel is presented in Figure 4. It should be mentioned that since a whole wafer will go through the DRIE process, the depth of all the samples will be the same.

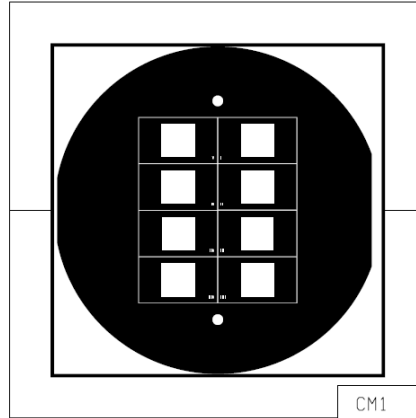


Figure 4: CAD drawing of the mask used for patterning the microchannel.

3.4 Manifold Design

Flow distributors were designed to have outlet width twice the inlet width. The same as the microchannel fabrication, all manifolds had have same depth of 500 μm .

Dimensions of the manifold are listed in Table 2.

Table 2: Geometrical dimension of the manifold.

Inlet Width (μm)	120	120
Outlet Width (μm)	240	240
Depth (μm)	500	500
# Manifold/ cm	25	25
Number of inlet flow	13	13
Number of outlet flow	13	13

It should be mentioned that two microfabrication masks were needed for the manifolds, since on one side of the silicon wafer the flow distributor were fabricated and on the other side the inlet and outlet holes should be fabricated. Also since the goal was to keep the number of manifold per centimeter constant for comparison purposes, the wall thickness is changed in these two designs. A schematic view of the manifold and microchannel is presented in Figure 5.

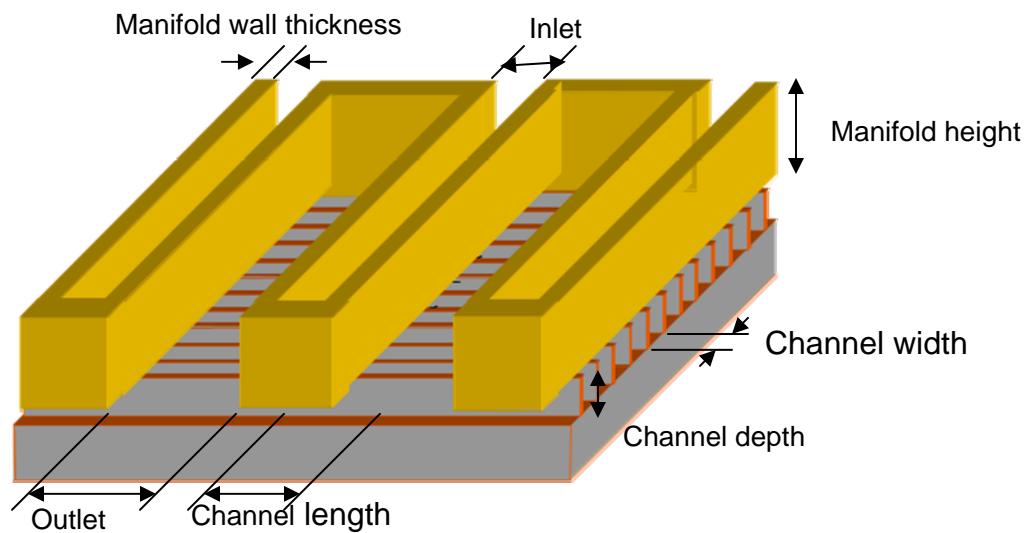


Figure 5: Schematic drawing of the manifold.

The microfabrication mask layout for the manifold is presented in Figure 6 and for inlet and outlet holes is presented in Figure 7.

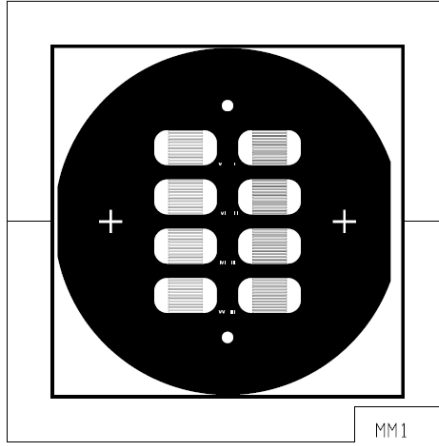


Figure 6: CAD drawing of the mask used for patterning the manifold.

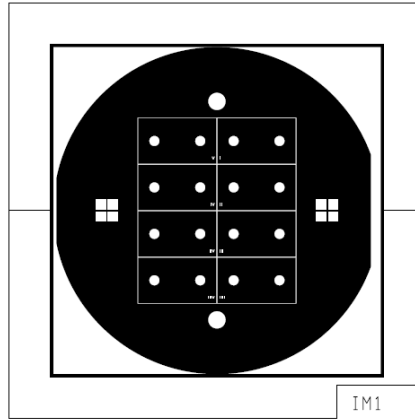


Figure 7: CAD drawing of the mask used for patterning inlet and outlet holes.

3.5 Heater Design

To simulate the heated surface, a resistance was designed to have resistivity of around $70 \, \Omega$. A serpentine gold heater was designed with thickness of $500 \, \text{\AA}$ and total length of $8 \, \text{cm}$. Two $1.5 \times 1.5 \, \text{mm}$ square areas were added to both sides of the heater, which served as a wirebonding place. A schematic view of the heater is presented in Figure 8.

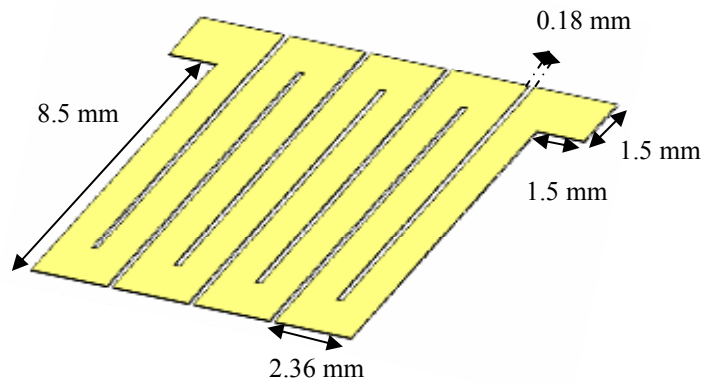


Figure 8: Schematic drawing of the heater.

For fabrication of the heater a mask layout was designed in AutoCAD and is presented in Figure 9.

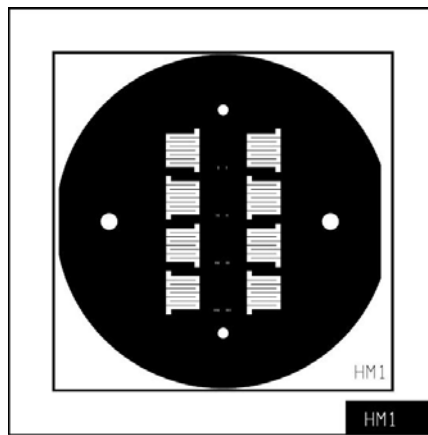


Figure 9: CAD drawing of the mask used for patterning the heater.

3.6 Package Size

The package housing was designed using G10 in which to place the cooler sample. The housing has 3.2 mm inlet and outlet holes for the flow and a metal pad for the

electrical connection of the resistor. In Figure 10 an AutoCAD drawing of the housing is presented.

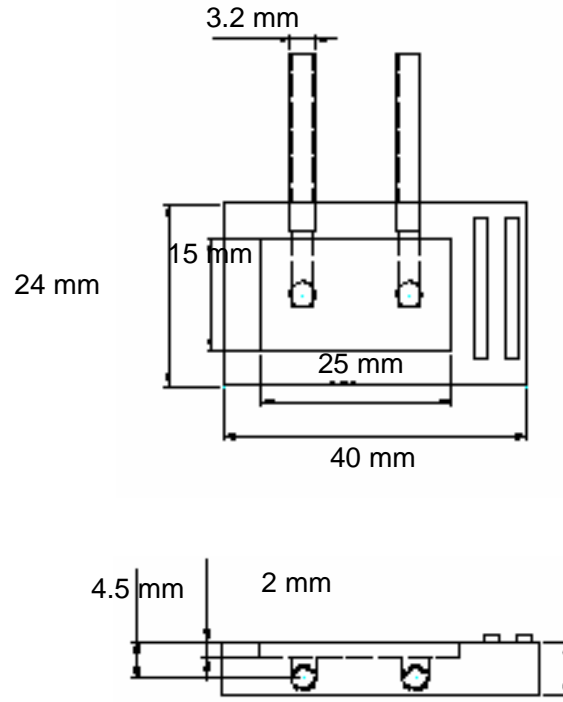


Figure 10: CAD drawing of the housing.

3.7 Numerical Analysis

The goal of this numerical study was to obtain a better understanding of the manifold microchannel cooling process on microchannel surfaces. As a modeling tool, the Fluent® CFD solver was used. It is widely accepted as one of the most advanced numerical modeling software packages for fluid flow problems. In this study water was used as the working fluid and silicon was the microchannel material.

In this study the main focus was on performance of the microchannel structure operating in a single-phase mode. One quarter of the microchannel structure element and manifold was modeled as a 3D computational domain to reduce the computation time. A constant heat flux of 100 W/cm^2 was imposed as the boundary condition. Water at $300 \text{ }^{\circ}\text{K}$ inlet temperature was used as the working fluid. The microchannels with two different aspect ratios of 10.0 and 2.5 were modeled as a base case for the study. In both designs the number of manifolds per centimeter was 25 but for two different designs, inlet equal to outlet and outlet twice the inlet. The major evaluating parameter was base temperature and also heat transfer coefficient to maintain such heat removal.

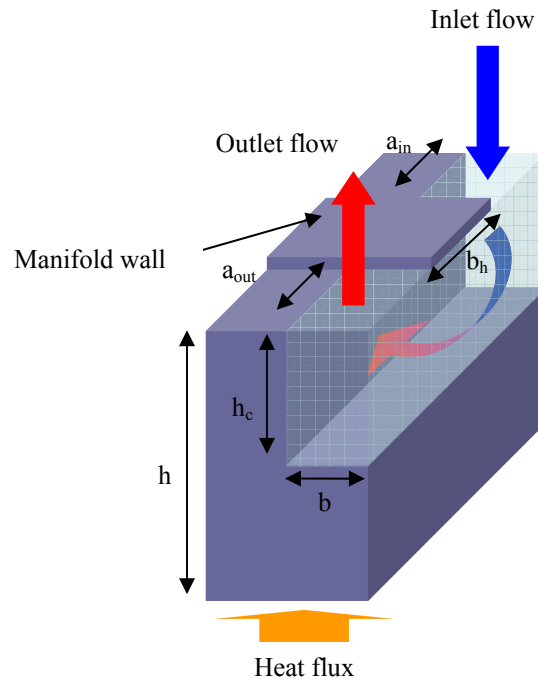


Figure 11: Computational domain.

Figure 11 presents a schematic view of the computational domain for the manifold microchannel heat transfer structure and the boundary conditions that determine heat transfer and fluid flow. During the computations, the following geometric parameters were kept constant: domain height, $h = 500 \text{ } \mu\text{m}$; channel height, $h_c = 200 \text{ } \mu\text{m}$; flow outlet lengths, $a_{\text{out}} = 240 \text{ } \mu\text{m}$. Boundary condition was constant heat flux to the base of the domain. The varied parameters were channel width, b ; and manifold wall thickness, b_h and inlet flow length a_{in} .

The geometry of the microchannel surface used in the simulation was similar to the surface, which was fabricated in the Fabrication Laboratory at the University of Maryland, as will be discussed in Chapter Four. The first modeled case was $20 \text{ } \mu\text{m}$ width channel and $200 \text{ } \mu\text{m}$ depth. Half of the inlet value as used in the quarter-element computational domain. In this simulation the fin thickness was equal to channel thickness.

Figure 12 presents the numerical result of the flow velocity in the computational domain for the channel width of $20 \text{ } \mu\text{m}$, and inlet flow distributor equals the outlet (inlet and outlet wall thickness are $240 \text{ } \mu\text{m}$ and the distributor wall thickness is $160 \text{ } \mu\text{m}$). The maximum coolant velocity is 2.15 m/s . As seen in Figure 13, fluid in the areas with low velocity heated up. The average base temperature was 305 K . The required pumping power to cool the plate of 100 W/cm^2 was 1.75 W . The nominal area heat transfer coefficient was calculated by dividing the heat flux through the base area by the temperature difference between the average base surface temperature and

the average of inlet and outlet fluid temperatures. The calculated nominal area heat transfer coefficient for the geometry number 1 is 239808 W/m²K.

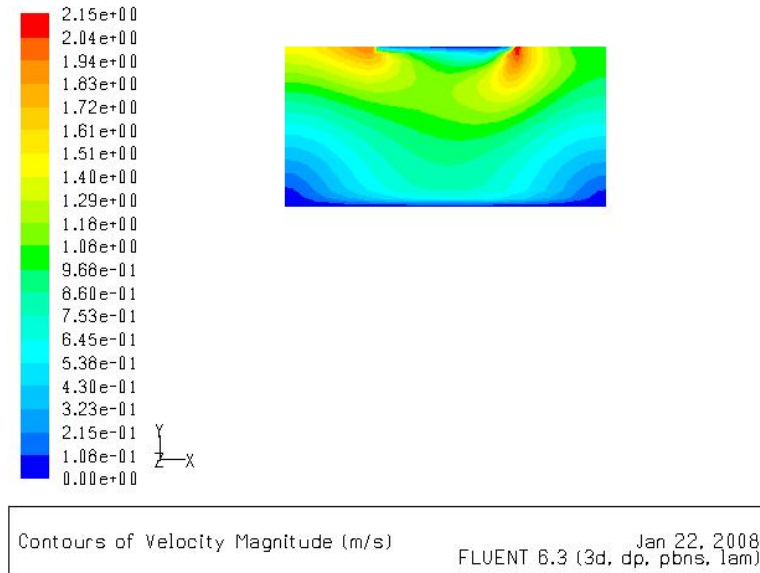


Figure 12: Velocity distribution in the fluid domain for the first design with channel width of 20 μ m and equal inlet and outlet.

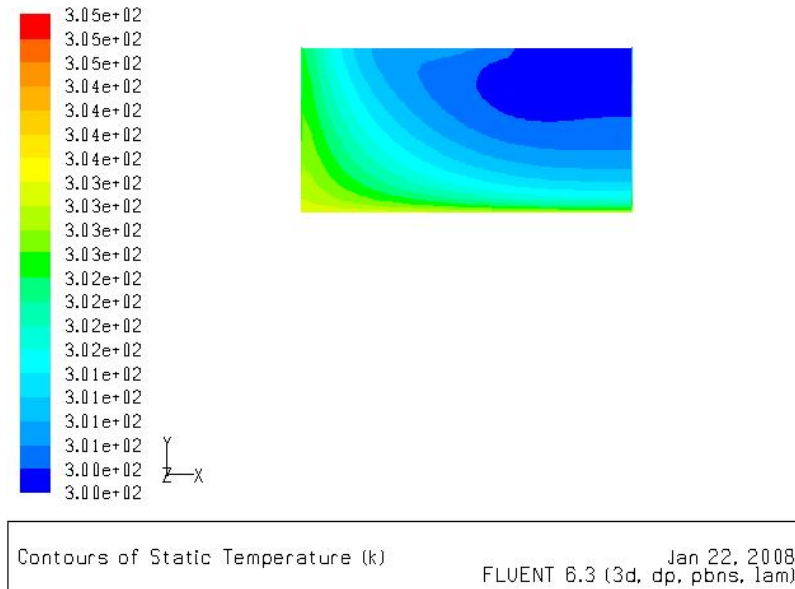


Figure 13: Temperature distribution in fluid domain for first design with channel width of 20 μ m and equal inlet and outlet.

Figure 14 and Figure 15 present the fluid velocity and temperature distribution in the fluid and the microchannel comprised from the same microgroove surface but with the inlet feeder thickness at half the outlet in the flow distributor. To keep the number of manifolds per centimeter constant, in this modeling the wall thickness of the distributor increased to 220 μm and inlet decreased to 120 μm . The boundary conditions were kept similar in these geometries. This increase in wall thickness resulted in an increase of maximum flow velocity to 2.24 m/s and a decrease in nominal area heat transfer coefficient to 229621 $\text{W}/\text{m}^2\text{K}$. As a result, the average wall temperature increased to 305.5 K while the required pumping power decreased to 1.23 W.

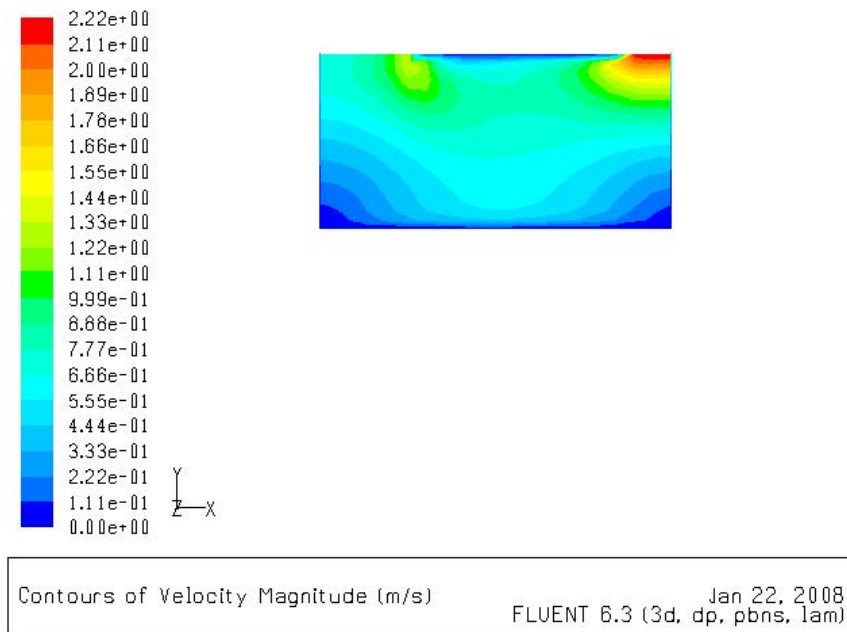


Figure 14: Velocity distribution in the fluid domain for the first design with channel width of 20 μm and outlet twice the inlet.

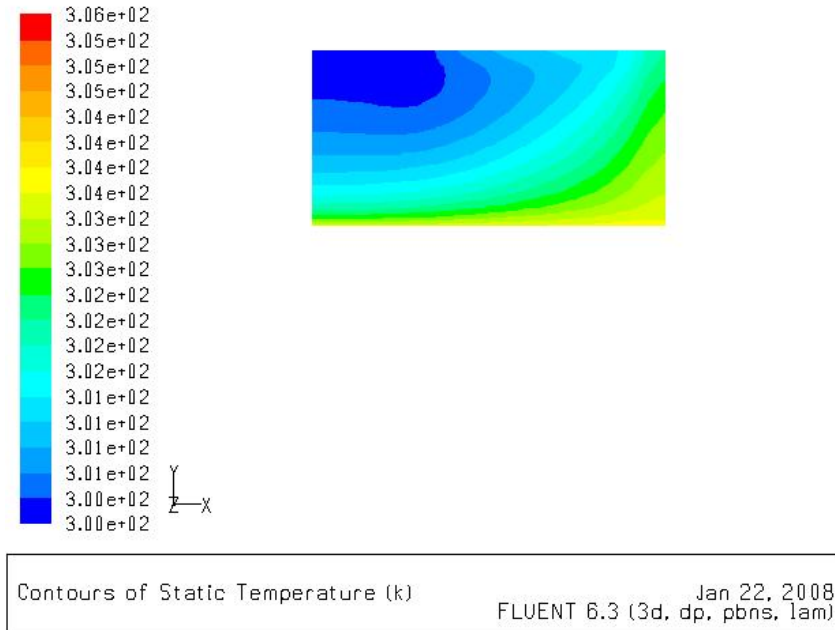


Figure 15: Temperature distribution in fluid domain for the first design with channel width of 20 μm and outlet twice the inlet.

Next, the aspect ratio of the microchannel was decreased from 10 to 2.5 for a constant channel depth, as depicted in Figure 16 and Figure 17. This study was done for the case where thickness of the inlet flow distributor equals the thickness of the outlet flow distributor (inlet and outlet wall thicknesses were 240 μm and the distributor wall thickness was 160 μm). Decreasing the channel aspect ratio for similar boundary conditions affects the flow configuration and velocities. This resulted in increased velocity to 3.84 m/s and a 1.7 degree increase in base temperature compared to the microchannel with width of 20 μm . But it also increased required pumping power to 3.89 W.

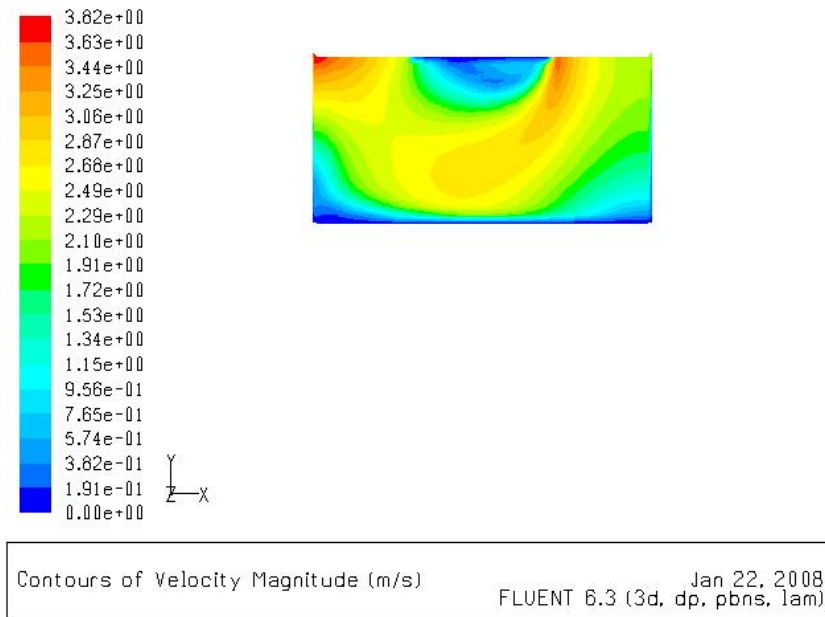


Figure 16: Velocity distribution in the fluid domain for the first design with channel width of 80 μm and inlet equals outlet.

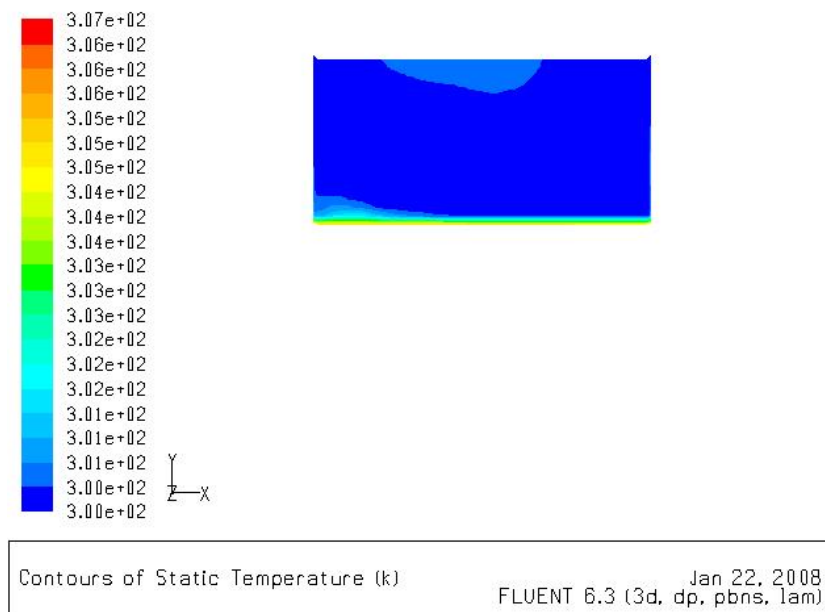


Figure 17: Temperature distribution in fluid domain for first design with channel width of 80 μm and inlet equals the outlet.

The same comparison is shown for this channel in Figure 18 and Figure 19 for inlet wall thickness half of the outlet wall thickness. Here again, to keep the number of

manifolds per centimeter constant the distributor wall thickness increased to 220 μm and inlet wall thickness decreased to 120 μm . Such increase in wall thickness and decrease in outlet resulted in an increase of maximum flow velocity to 4.06 m/s and decrease in nominal area heat transfer coefficient to 145349 W/m²K. As a result, the average wall temperature increased to 307.75 K while the required pumping power decreased to 2.37 W.

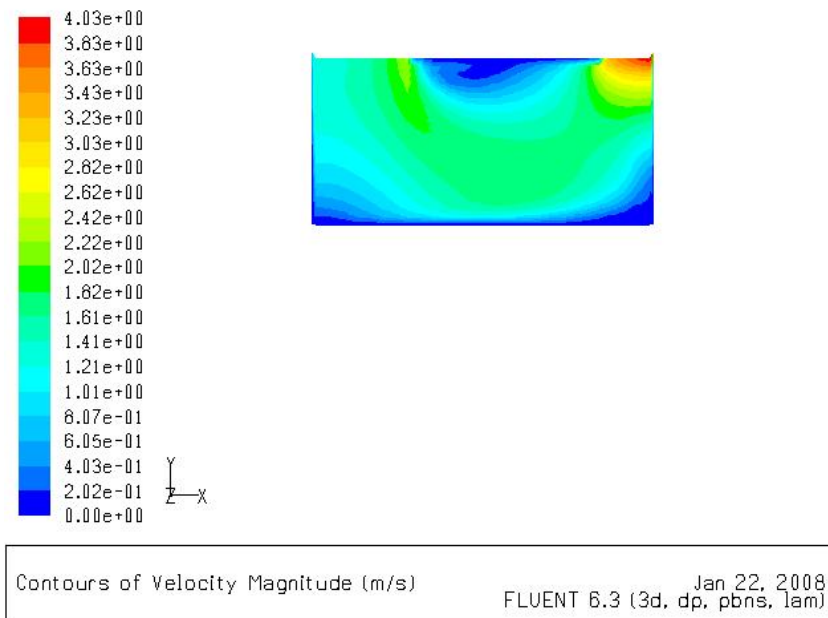


Figure 18: Velocity distribution in the fluid domain for first design with channel width of 80 μm and outlet twice the inlet.

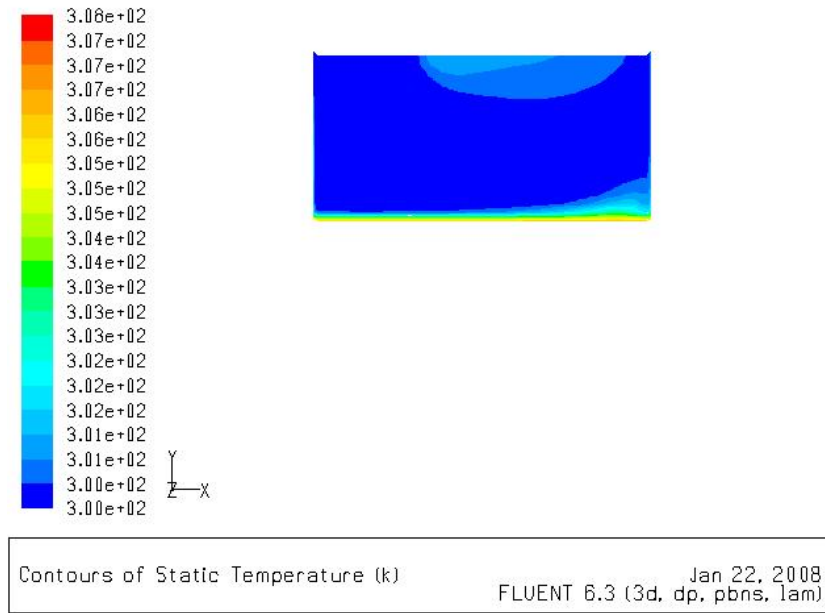


Figure 19: Temperature distribution in fluid domain for first design with channel width of 80 μm and outlet twice the inlet.

Table3 summarizes the results of the current computational analysis. In all of the configurations the number of manifolds per centimeter was 25. In the first and third designs the inlet and outlet were equal to 240 μm but in second and forth one the inlet was half the outlet, in which case the manifold wall was thickened. Moreover, the first and second designs were for channels with aspect ratio of 10, while the third and forth designs were for a channel-width aspect ratio of 2.5. Comparing the first and second designs, it can be concluded that for designs in which the inlet is smaller than the outlet, maximum flow velocity increases and pressure loss in manifold decreases, so the pumping power decreases too. However, the nominal heat transfer coefficient decreases and the base temperature increases. For high aspect ratio channels with a high number of channels per centimeter, it seems that having the inlet equal the outlet increases the heat transfer coefficient, and the increase in base temperature is not significant.

Configurations 3 and 4 were developed for the purpose of reducing the aspect ratio while keeping the heat transfer parameters at the desired level. The geometry of the manifolds used in those iterations is similar to that in first and second, but the aspect ratio was reduced to 2.5, resulting in a decrease in the number of channels per centimeter from 250 to 62. As a result, it can be concluded that for lower aspect ratios, if outlet is bigger than inlet, base temperature increases and heat transfer coefficient decreases accordingly.

The changes in geometry of the microgrooved surface and the feed channel explored in this study indicate uniform and higher heat transfer occurs for higher numbers of channel per centimeter, and for this design making the inlet smaller than the outlet can decrease required pumping power due to decrease in fluid mass flow.

Table3: Effect of change in computational element geometry on heat transfer at constant heat flux of 100 W/cm²

Parameters					
		1	2	3	4
Inputs	Channel depth, (μm)	200	200	200	200
	Channel width, (μm)	20	20	80	80
	Inlet width, (μm)	240	120	240	120
	Outlet width, (μm)	240	240	240	240
Results	Base Temperature (K)	305	305.46	306.7	307.75
	Heat transfer coefficient, (W/m²K)	239808	229621	163934	145348
	Maximum flow velocity (m/s)	2.15	2.24	3.84	4.06
	Pumping power (W)	1.75	1.23	3.89	2.37

3.8 Summary

The design strategy of the manifold microchannel for concentrated solar cell cooling was described in the first part of this chapter. Geometrical design parameters of different devices used in the experiments were presented next. Finally, results of the fundamental numerical modeling to better understand the flow pattern in the manifold and microchannel were described. Numerical modeling results helped to better understand the characteristics of manifold microchannel technology.

The next chapter will provide information on the micro-fabrication of the different devices described in this chapter.

Chapter 4: Fabrication Process

4.1 Introduction

The materials and fabrication processes for making the microchannels and manifolds were selected based on their particular properties and characteristics, as well their manufacturability. For the stacked test sample as discussed in the previous chapter, a silicon wafer substrate was selected because solar cells are made of silicon; therefore there will be zero thermal resistance between the microchannel and heated surface.

On the other hand, silicon has a thermal conductivity of 148 W/mK, which is relatively high. But it is much less expensive than diamond, which has high thermal conductivity. Moreover, microfabrication on silicon substrate is well developed and advanced in MEMS technology [27], [28].

In the current research, the microchannel structure was fabricated on 4" diameter, 0.5 mm thickness double-sided polished silicon wafers, and the manifolds were fabricated on 1.0 mm thickness double-sided polished silicon wafers. Both sides of the wafers contained a layer of thermally grown silicon oxide. Because they are double-sided wafers, photolithography can be performed on both faces of the wafers. Details of the main steps of micro-fabrication techniques are described in the following sections. In Table 4 the fabrication steps are schematically presented.

4.2 Photolithography to Generate the Pattern

The process started with cleaning the wafer with methanol and acetone and then nitrogen to dry the wafer. It is essential to have dry wafer surface for good adhesion of photoresist, so the wafer was baked for 3 minutes on a 120 °C hot plate immediately prior to the photoresist application (Step (a) in Table 4). Additional surface treatment with hexamethyldisilazane (HMDS) was necessary to promote adhesion of the photoresist to silicon oxide layer; therefore, the surface of the wafer was completely covered with HMDS. HMDS was spread at 4000 rpm for 40 seconds to cover the wafer. Then photoresist Shipley 4620 was dispensed on the wafer at 1500 rpm for 60 seconds to obtain a layer 13 µm thick. Then the wafer was soft-baked at 90 °C for 1 minute on hot plate.

Later the mask was aligned with the wafer and wafer was exposed to UV radiation in an EVG mask aligner for 100 seconds. The next step was development of the photoresist: the wafer was immersed in the 1:3 diluted microstrip 400K developer and rinsed immediately in water after 120 seconds. Before proceeding, the wafer was inspected under the filtered microscope to check the development. If development was insufficient, the process was repeated for another 40 seconds.

Before performing the wet etching of the oxide layer, since the wafer is double-sided and covered with an oxide layer, the backside oxide layer needed protection from wet etching. Therefore, the photolithography process was repeated again with HMDS and Shipley 1813 for 40 seconds to cover the backside with a layer 1.3 µm thick.

For etching the oxide layer wafer should be placed in BOE 6:1 for at least 10 minutes and rinsed in water. Then thickness of the oxide layer should be checked with profilometer. (Step (b) in Table 4)

4.3 Etching the Manifold on the Silicon Wafer using DRIE

Etching of parallel microchannels can be achieved with a chemical etching method such as wet etching or dry etching. In this work the deep reactive ion etching (DRIE) technique was used for both microchannels and manifolds. A standard Bosch process was implemented using an inductively coupled plasma (ICP) etcher in which RF induced plasma accelerates the free ions, causing a chemical reaction and the bombardment of the surfaces to be etched. Compared with a conventional RIE, ICP can achieve better anisotropy, as two power supplies are used to generate denser plasma and accelerate the free ions respectively [29].

The Bosch process includes three steps, which are repeated throughout the etching cycles. The first step is isotropic etching of the exposed area in the silicon wafer using SF_6 . A fluorinated polymer is subsequently deposited on both the trench sidewalls and bottom walls using C_4F_8 . In the third step, SF_6 is used to etch the polymer anisotropically, as it etches the bottom faster than the sidewalls. In the subsequent step, the sidewall is effectively protected by the polymer so that silicon etching only occurs at the bottom of the trench. With an appropriate masking layer, the Bosch process can be used to etch deep features with aspect ratios up to 20.

Since on one wafer both manifolds and inlet and outlet holes exist, etching has to be done in two steps. Manifolds are etched initially to a certain depth. Inlet and outlet holes are etched in the second step until the holes are through. The two etching steps should be performed on opposite sides of the wafer. For that, backside alignment is necessary for the photolithography of the second step.

In this work the second method was used, in which two etching steps were performed on different sides of the wafer. Since the exact etch rate of silicon was unknown, the etch rate was first found on a dummy wafer; the etch rate was about $2.4 \mu\text{m} / \text{minutes}$. The front side (manifold design) was etched in 4 steps. The first 3 took 60 minutes each and the last took 40 minutes to reach the total depth of $500 \mu\text{m}$ for the manifolds (Step (c) in Table 4). In Figure 20 the silicon wafer front side after wet etching of the manifold is presented.

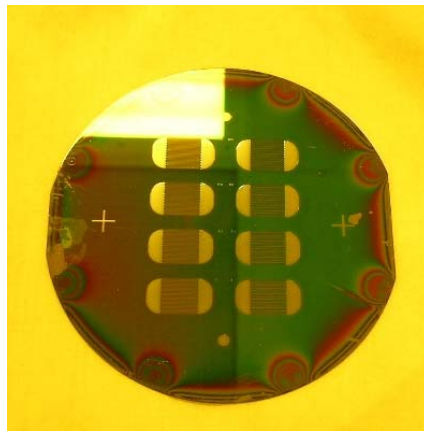


Figure 20: Picture of the manifold wafer after DRIE.

4.4 Etching the Inlet and Outlet holes in the Silicon wafer Using DRIE

For patterning the backside, first the resist should be striped, which is used as a mask for wet etching of the front side so the oxide layer on the backside will not be etched during the processes. Therefore resist was striped with acetone. Again the back side was covered with photo resist and exposed under the EVG mask aligner for another 100 seconds and developed using the same processes in the 400K developer.

Once the backside design was completely developed and ready for wet etching to remove the oxide layer, the front side design was covered with photo resist in the same manner to avoid the front side oxide layer from etching.

It is noted here that during ICP etching the wafer was cooled from the backside with a helium flow. This is important to protect the photo-resist integrity. When there are through features, there will be helium leakage, which can cause the machine to shut down, as helium pressure is not able to be maintained. To prevent this, the working wafer was bonded to a carrier wafer using a thin photoresist layer. Therefore, after three hours etching, the wafer was taken out and a pilot wafer was stuck to it with a little photoresist and baked in a 100 °C oven for an hour. Again the DRIE was continued until the holes came through the wafer. Then, to separate the two wafers they were rinsed in micro-strip for an hour or two until the stripper could go through all the holes (Step (d) in Table 4). In Figure 21 the backside of the silicon wafer with inlet and outlet holes is presented. In Figure 22 the front side of silicon wafer with the manifold is presented

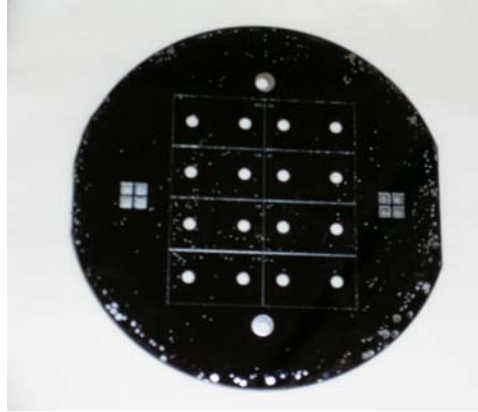


Figure 21: Picture of the back side of manifold wafer after inlet and outlet holes etched.

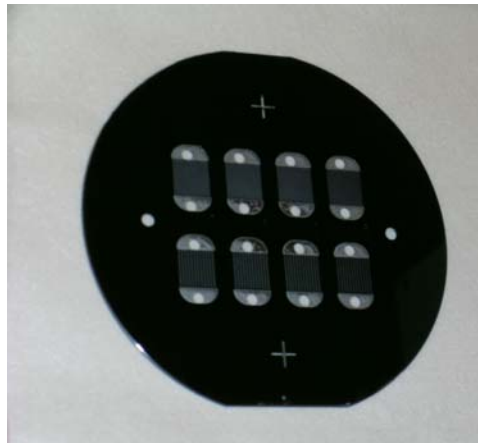


Figure 22: Picture of a completed manifold wafer.

4.5 Etching Microchannel in the Silicon Wafer Using DRIE

Following similar steps, the microchannel was also fabricated on silicon wafers. Microfabrication of the microchannel followed the same process as the manifold, except that instead of Shipley 4620, resist 1813 was used, which is strong enough for 200 μm depth. The wafer was then exposed under the EVG mask aligner for 40 seconds and etched for a total time of 70 minutes (Step (e) and (f) in Table 4). In Figure 23 the microchannel wafer after DRIE is presented.

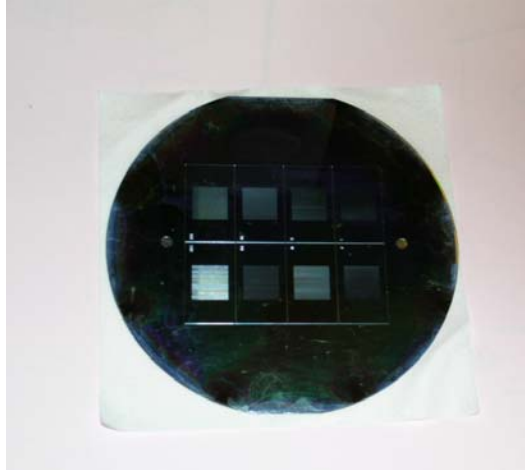


Figure 23: Picture of the microchannel silicon wafer after DRIE.

4.6 Scan Electron Microscopy (SEM)

A scan electron microscope (SEM) forms a three-dimensional image on a cathode-ray tube by moving a beam of focused electrons across an object and reading both the electrons scattered by the object and the secondary electrons produced by it. The main goal of SEM photography in this study was to inspect the sidewalls for micro-defects as well as the roughness of the bottom surfaces. The DRIE technique was intended to produce vertical side walls without taper and inclination. As can be seen in Figure 24 and Figure 25 the verticality of the walls was properly achieved and no significant inclination is visible. Moreover, the bottom surfaces of the channels are relatively smooth. It should be mentioned that each channel had 200 μm depth and 20, and 40 μm widths.

Figure 26 and Figure 27 show the SEM photographs of the manifold. As seen there, some micro-needles were created on the bottom face of the manifold wafer. The

reason for formation of microneedles is unclear; however, it seems that these needles are formed due to the high etching depth (500 μm) and the low quality of mask layer. The needles are more concentrated in the corner regions. In order to remove them, the sample was sinked in an ultrasonic bath, causing them to break by vibration to improve the surface smoothness

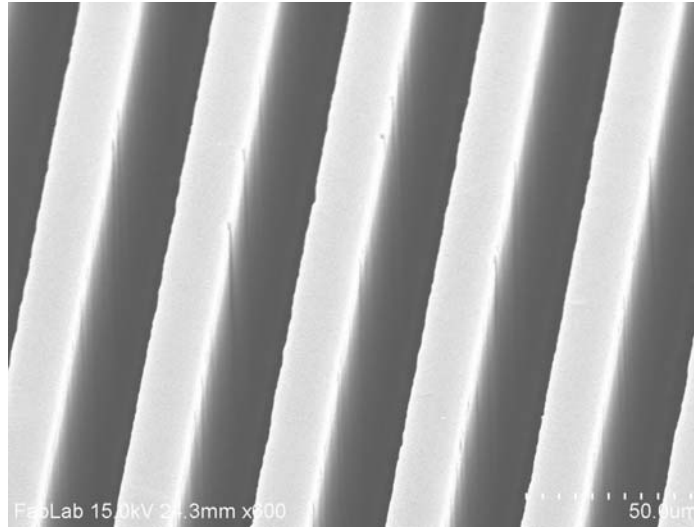


Figure 24: SEM image of the 20 μm width microchannel.

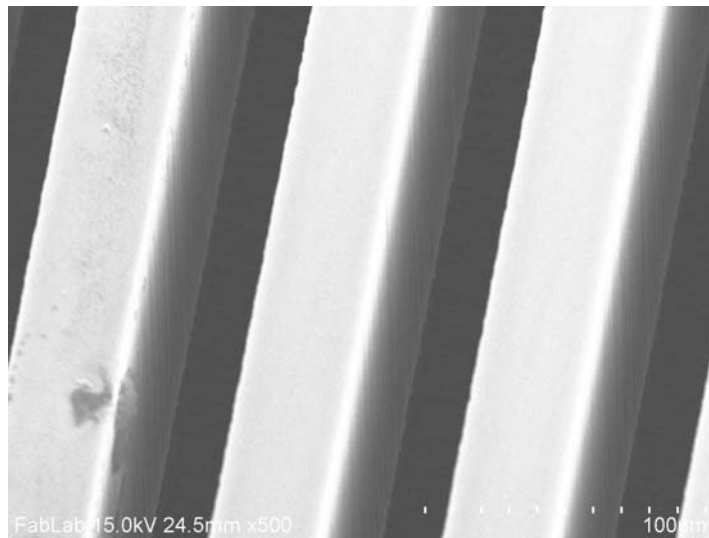


Figure 25: SEM image of the 40 μm width microchannel.

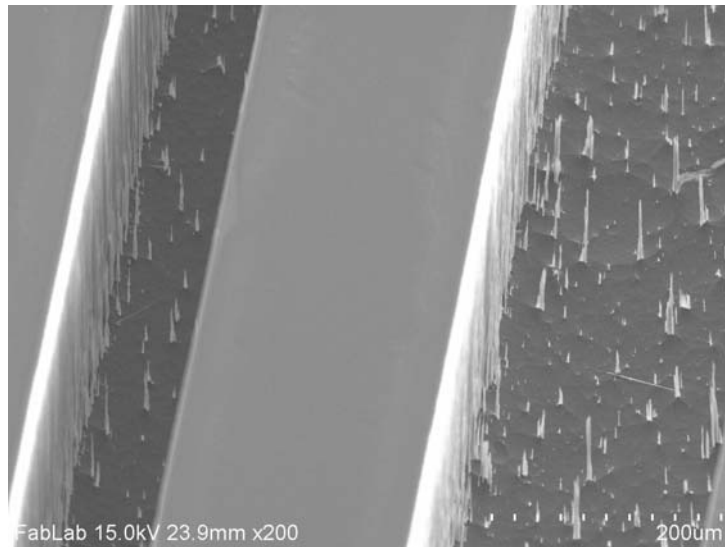


Figure 26: SEM image of the manifold wall.

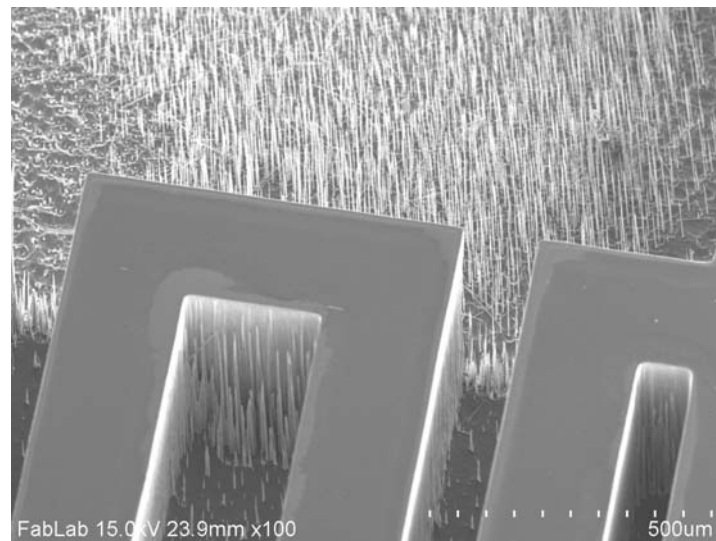


Figure 27: SEM image of the manifold corner.

4.7 Bonding of Microchannel Wafer and Manifold Wafer

There are two types of bonding methods available for the current work [30], [31].

One of them is eutectic bonding and the other one is direct bonding. Direct silicon-

silicon bonding without intermediate layer is achieved by placing the surfaces of two wafers in close contact and inserting them in an oxidizing ambient. The quality of this bond is highly dependent on temperature and roughness of the surfaces. In this bond, flatness of surface is critical, which is difficult to achieve for this study, where all the surfaces have gone through the DRIE process and have rough surfaces. Therefore, for this study the eutectic bond was chosen. This type of bond uses metals as an intermediate layer to form eutectic bond between the microchannel silicon wafer and manifold silicon wafer.

The typical bonding procedure started with wafer cleaning and oxygen plasma exposure to have completely clean surface. Then, a number of stacked metal layers were deposited on both sides of the microchannel and manifold wafers using an e-Beam evaporator. These layers were designed to serve as bonding layers for the AgSn eutectic bonds. The composition of the metal layers was as following: 100 \AA chromium, 10000 \AA silver, 2000 \AA tin, and 500 \AA gold. The chromium served as an adhesion layer between the metal layers and silicon oxide, and the gold layer acted as a corrosion and oxidation barrier. The first bonding trial with the whole wafers in a non-vacuumed oven at 350 $^{\circ}\text{C}$ was not successful because the tin oxidized. The next trial was performed on small pieces of experimental wafers in two different furnaces at 600 $^{\circ}\text{C}$ and 800 $^{\circ}\text{C}$. In Figure 28 the sample bonded in the 800 $^{\circ}\text{C}$ furnace is shown. After separating the wafers, as seen, the metal layer was not strong enough, and the temperature was very high. In Figure 29 the sample bonded in the 600 $^{\circ}\text{C}$ furnace is

shown. After separating, this sample shows some gaps in the metal which could be due to the lack of vacuum environment and pressure in the furnace.

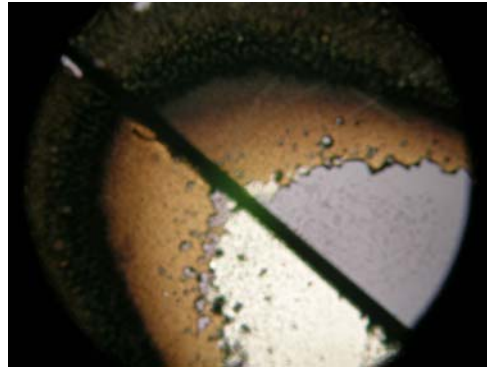


Figure 28: Image of the sample wafer bonded in 800 °C.

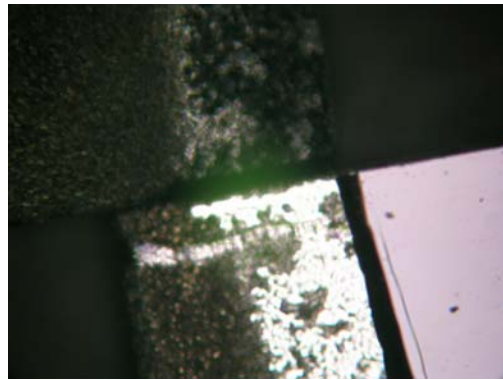


Figure 29: Image of a wafer bonded in 600 °C.

In another trial the thickness of the metal stack was changed, the silver thickness increased to 2 μm and tin increased to 2 μm . This trial was carried out in a furnace at 600 °C but without nitrogen and oxygen to reduce the existence of any air gaps between the metal layers. Moreover, the silicon wafers were cut using a wafer dicing saw across the etched dicing line provided for this purpose before bonding. In Figure 30, the samples with the metal stack before bonding are shown. To have uniform pressure on the sample in the furnace, each sample was cleaned and placed between

two Pyrex pieces, tied tightly with glass fibers, and then placed in the furnace (Step (g) in Table 4).

The bonded structure was examined in an X-ray machine. In Figure 31 an X-ray image of one of the samples is presented. This image was used to inspect the existence of voids and the quality of the bonded sample. As seen, the alignment between the two layers was good, judging from the shadow of the microchannels and the manifold. This figure also indicates some air gaps around the bottom hole, which was possible due to over-metallization at that point.

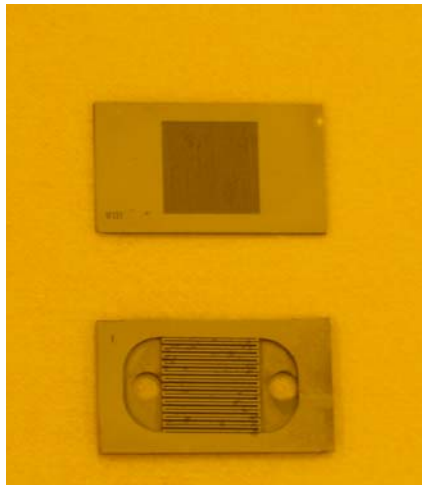


Figure 30: Two silicon wafer with deposited metal stack.

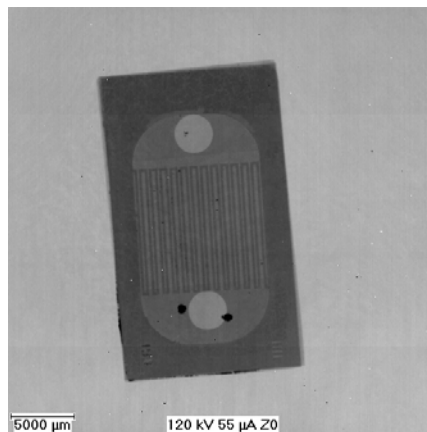


Figure 31: X-ray image of bonded wafers.

4.8 Microfabrication of Heater

The heater was micro-fabricated on the backside of the microchannel wafer after eutectic bonding to simulate the heated solar cell. This fabrication was done with a lift-off process ([27], [32]) as schematically illustrated in Figure 32. This is the easiest method because it involves only one mask step and the photolithography is completely standard. Prior to film deposition, particularly for sputtering or evaporation processes, a post-develop bake is recommended. This drives off excess solvent so that there will be less outgasing during the film deposition. However, the bake should not be too long or at too high temperature, otherwise the resist will reflow slightly.

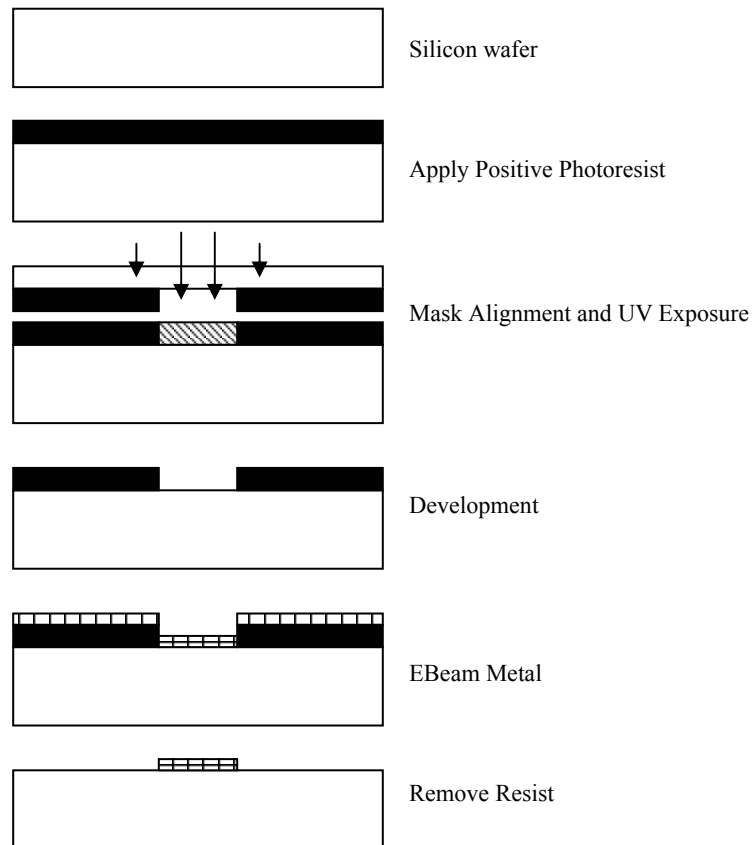


Figure 32: Lift off Sequence with positive photoresist [27].

The first step in making a heater is to cover the surface with an oxide layer to act as an insulator layer, but since the wafers were covered with oxide previously, the lift-off steps started with photolithography of the positive photoresist on the sample.

The process starts with cleaning the wafer; then the photolithography is done with Shipley 1813 in a similar manner and exposed under the EVG mask aligner for 40 seconds. Then the resist is developed in developer 352 for 60 seconds. Before the metal deposition, the wafer is post-baked for one minute. Later, metal deposition is done in an eBeam machine, and the final step is immersing the wafer in the acetone.

The length of time for lift-off depends on the film quality (generally, the higher the film quality, the more impermeable it is and the longer it will take to lift-off.). It is important to keep the substrate immersed in acetone until all the film has been lifted off and there are no traces of film particulates; once particles dry on the substrate, they are difficult to remove.

The first-generation design of the heater consisted of 100 \AA chromium as an adhesion layer and 1000 \AA platinum acting as the main resistive element. In Figure 33 a sample fabricated heater is presented. In order to limit the material cost and provide a more cost-effective solution for the heater, a second design of the heater was developed in which chromium was the adhesion layer but gold was the main resistance because gold has good resistance to oxidative corrosion. In the second design the thickness of the gold layer was 500 \AA . The resistances of the second

heater design were found to be between 70 and 80 Ω , matching the design requirements (Step (h) in Table 4). In Figure 33a sample of microfabricated serpentine gold heater is presented

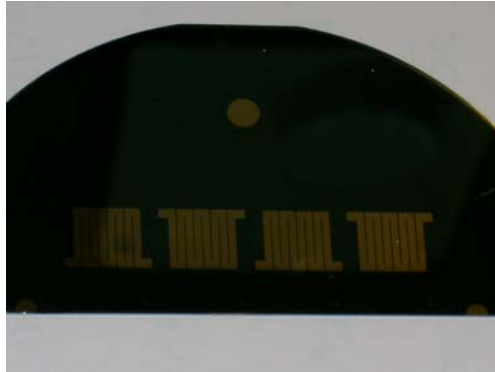



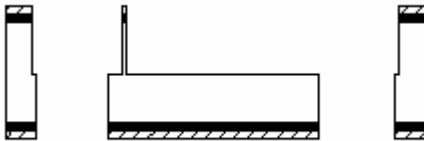

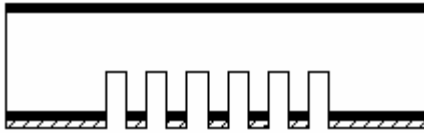
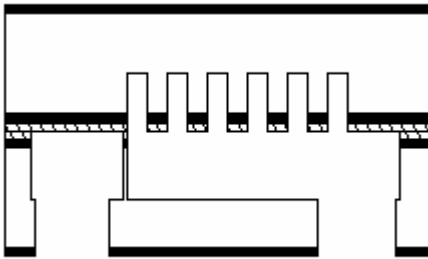
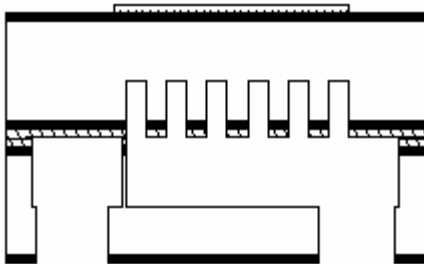







Figure 33: Image of a sample fabricated heater.

Table 4: Sequence of microfabrication procedure.

				
(a) Cross section of silicon wafer with oxide layer.	(b) Patterned photoresist and etched oxide layer			
				
(c) Deep Reactive Ion Etched Manifold	(d) Deep Reactive Ion Etched holes			
				
(e)Patterned photoresist and etched silicon oxide	(f) Deep Reactive Ion Etched microchannel			
				
(g) Bonded two silicon wafer	(h) Deposited heat on the bonded wafer			
 Silicon	 Oxide	 Photoresist	 Metal	 Heater

4.9 Packaging Procedure

For the experimental test a secure housing was needed to provide wirebonding, electrical connections, the inlet and outlet, and handling of the sample, since the silicon wafer is very fragile.

The housing was designed to secure and protect the sample. In this technique a box-shape package was produced from G10 with a place for the sample to rest, two holes for incoming and outgoing flows, and electrical connections for wire bonding pads. G10 laminate grades were produced by inserting continuous glass woven fabric impregnated with an epoxy resin binder while forming the sheet under high pressure. This material is used extensively in the electronics industry because its water absorption is extremely minimal and the G10 line of materials is not electrically conductive. It also exhibits superior mechanical and dimensional stability with a small coefficient of thermal expansion. In Figure 34 a picture of sample G10 box is presented



Figure 34: G10 housing with inlet and outlet connections.

Quick-dry epoxy adhesive was used around the perimeter of the sample to fix the sample in the housing, and two springs were used to keep the sample in place. Two thin rubber sheets were used under and above the sample to have smooth contact between the sample and G10 package. Two pipes connected to the inlet and outlet holes for the refrigerant to go through the sample and come out.

4.10 Wirebonding

Wirebonding is the dominant technology used for interconnection between chip and substrate in industry and has two forms of bond, ball bond and wedge bond. There are two main wires used in this technology, gold doped with copper or beryllium, or aluminum doped with silicon. Ball bonding is mostly used in gold-bond wires in thermosonic bond machines at temperatures between 125 °C to 240 °C. However, for aluminum wires ultrasonic bonding is the dominant method.

In this investigation, wirebonding between heater gold layer and steel pad was needed to make electrical connections. For this purpose, the wirebonding machine at the Center for Nanophysics and Advanced Materials (CNAM) was used to make interconnections between the heater and the solder leads. In this study aluminum wire was attached to the gold heater at ambient temperature, and the wedge bond was formed by pressure and vibration energy. On each sample a minimum of 10 wirebonds were formed on each side to prevent wire burnout at high current tests.

In wire burnout, the current-carrying capacity of wire is exceeded and disconnects the wire due to metalurgical fatigue. The factors affecting wire burnout include resistivity, thermal conductivity, temperature coefficient of resistance, and melting point. Another major contributor is the length of the wire (the longer the wire, the lower the current needed for burnout). Since predicting wire burnout is difficult, over-specifying wire diameter or using multiple wires is common in this field, and therefore this study attempted to make as many wirebonds as possible considering the area allocated for this purpose on the heater. In this study one-mil diameter aluminum wire is used for wire connections that have been shown to have a burnout current of 0.4 amps for 1 cm length [33]. Figure 35 demonstrates a sample after packaging with wirebond on both sides and three K-type thermocouples to measure the temperature of the heater surface and two inlet and outlet thermocouples.

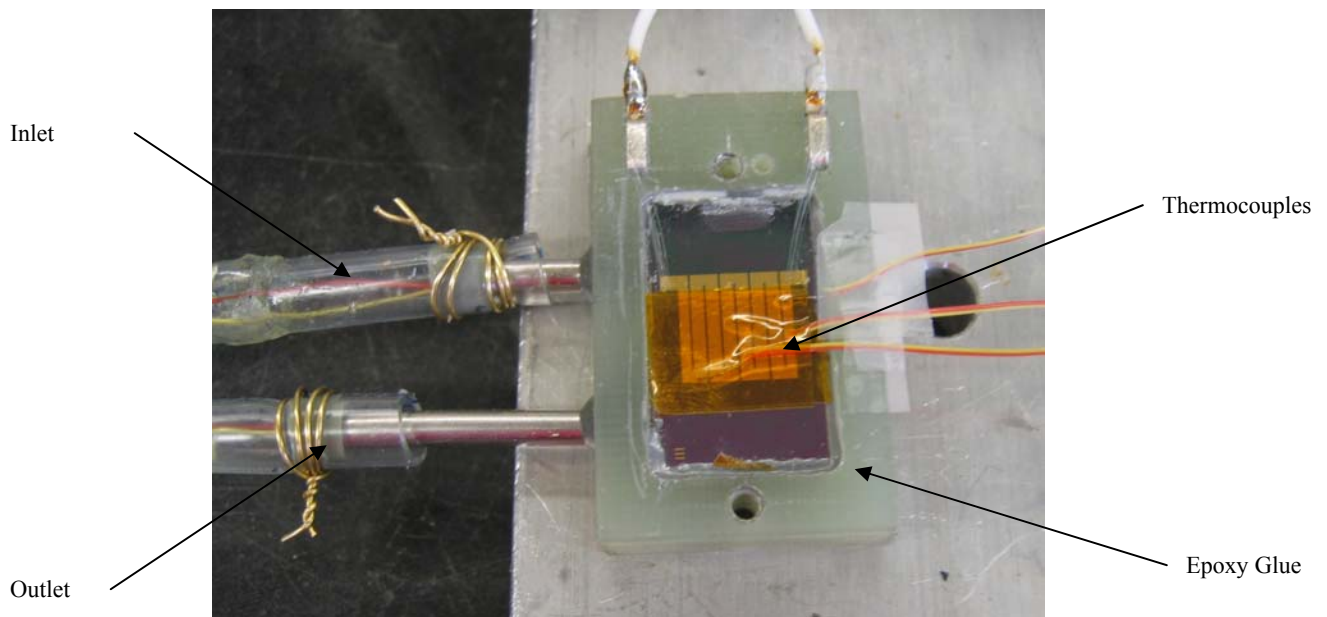


Figure 35: Packaged sample with thermocouples and electrical connections.

4.11 Summary

In this chapter, based on the design requirements discussed in the previous chapter, the micro-fabrication steps of the manifold, microchannels, and the heater were completely described, and two final samples were packaged as described in the packaging section. In the next chapter (Chapter 5) the experimental apparatus will be described and the heat transfer and pressure drop results obtained will be presented.

Chapter 5: Experimental Setup and Results

5.1 Introduction

A set of experiments was conducted in this study focusing on the heat transfer and pressure drop characteristics of the manifold microchannel structure. Thermal performance of the manifold microchannel was evaluated in a single-phase open loop system. The following sections detail the experimental setup and instrumentation. Experimental procedures will be discussed, followed by presentation of the results of the experiments on the two different samples tested in this study.

5.2 Instruments and Measurement Devices

A schematic of the experimental setup and corresponding apparatus is shown in Figure 36. De-ionized (DI) water is pressed by the nitrogen gas through a filter from the reservoir to the test module. The cold DI water picks up the heat from the manifold microchannel heat sink and returns to a collection container. The pressure of the water tank is controlled by high-precision pressure regulator valve located on top of the nitrogen gas tank. A U-type pressure gage is used to monitor the pressure drop across the test module. The steady water-mass flow rate was determined by weighing the mass of water over a long period of time using a high-precision electronic balance with accuracy of 0.05 g. The inlet and outlet temperature were measured by K-type thermocouples with a measurement error in the range of ± 0.3 °C.

The gold resistor was driven by a precision DC power supply unit (Sorenson, Inc., model #DLM150-4) to provide a uniform heat flux. The actual power input to the heater was determined by measuring the current through and the voltage across the heaters. The heat generated by the heater was transferred to the working fluid flowing through the microchannels. The temperature of the heater was measured with three K-type thermocouples.

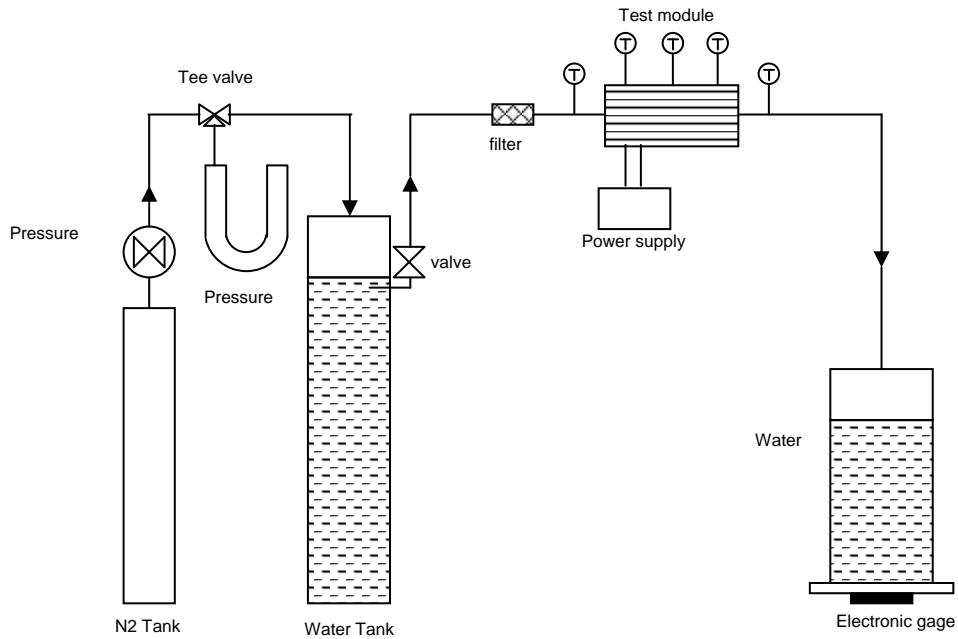


Figure 36: Schematic of test setup.

The power supply was controlled by a data acquisition system (BenchLink Data Logger System) programmed on a personal computer through a general programming interface bus DAS card. Data acquired through five thermocouples, a programmable power supply and BenchLink Data Logger System. A picture of the setup is presented in Figure 37.

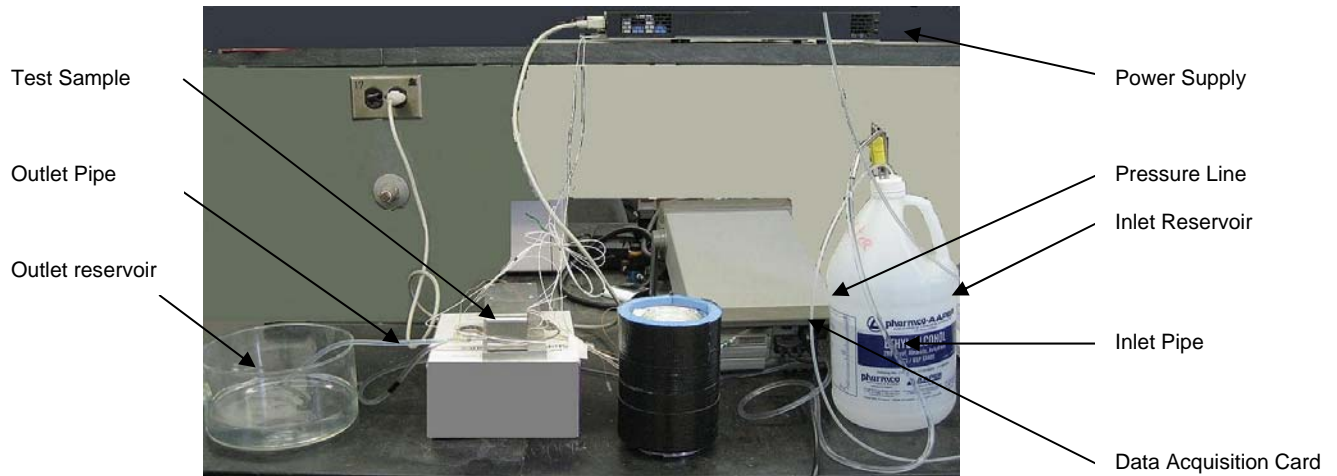


Figure 37: Picture of test setup.

5.2.1 Calibration of Thermocouples

The inlet and outlet water temperatures and heater surface temperature were measured using K-type thermocouples. The thermocouples were calibrated against the resistance temperature detector (RTD) in a temperature-controlled bath circulator.

The bath temperature was changed gradually, and at each step the temperature measured by the thermocouples and RTD were recorded simultaneously with temperature range between 10 °C and 60 °C to an uncertainty of ± 0.1 °C.

Considering the accuracy of the RTD, it was determined that the accuracy of the temperature measurement using thermocouples was in the range of 0.2 °C. The result of the calibration for one of the thermocouples is presented in Figure 38. As expected, a linear calibration curve was obtained.

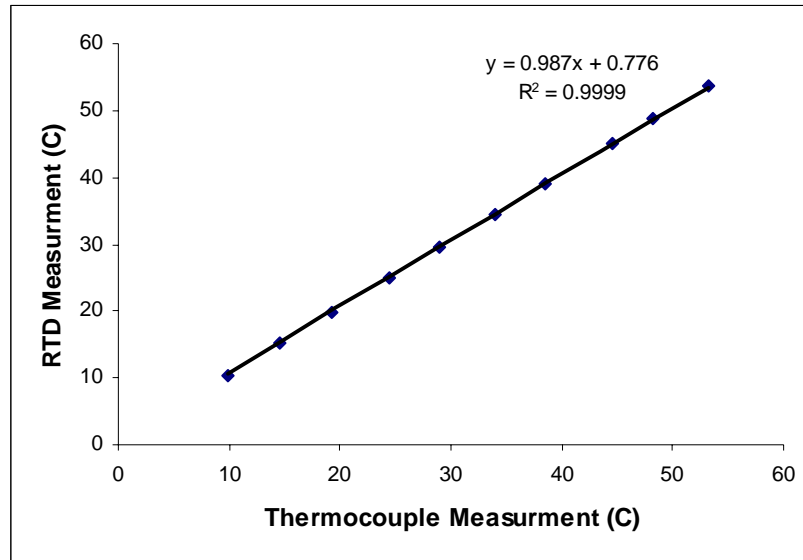


Figure 38: Thermocouple Calibration Curve.

5.3 Test Module

The test module, illustrated in Figure 39 consists of two layers of silicon plates. One microchannel layer at the bottom provides the cooling, and one manifold layer on top distributes the fluid. The gold heater is fabricated on top to represent the heat generation module. The microchannel, manifolds, inlet and outlet ports were all fabricated using the deep reactive ion etching (DRIE) technique. Two layers of silicon plate were bonded into a stack through a eutectic bond procedure. For this thesis two samples were fabricated and tested. The geometrical dimensions of these two manifold microchannels are presented in Table 5.

Table 5: Geometrical dimension of the samples tested.

	D_h (μm)	Microchannel length (μm)	Aspect Ratio	# Inlet Flow	# Outlet Flow
Sample 1	67	200	5	13	13
Sample 2	36	200	10	13	13

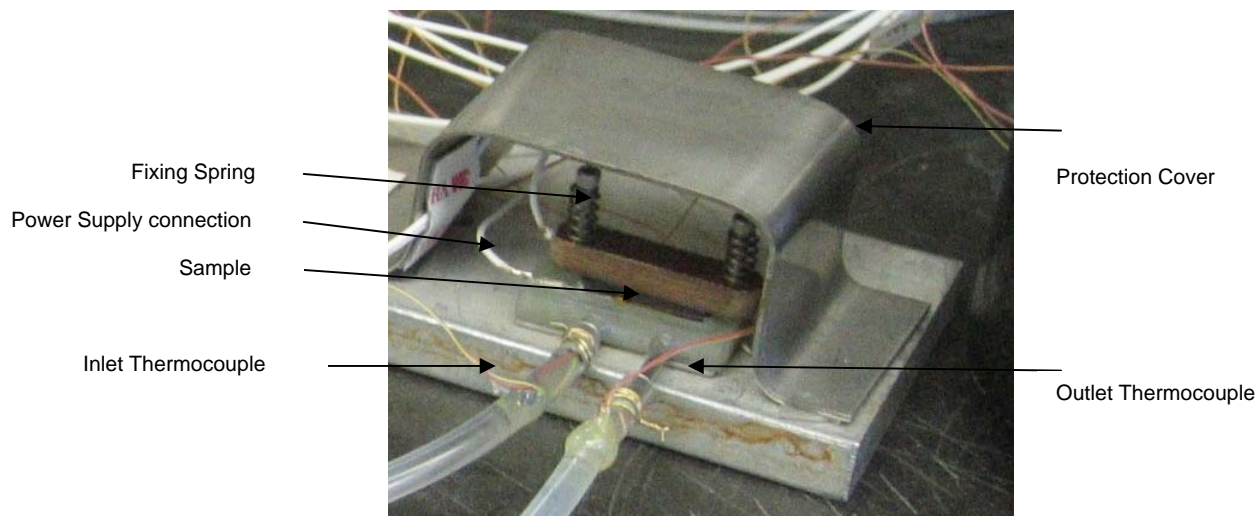


Figure 39: Picture of test module.

5.4 Experimental Procedure

A typical test run starts from degassing process. The trapped air was removed from the loop by running the system continuously for about 30 minutes. In the current experiments, the overall flow rate ranges from 0.3 g/s to 1.3 g/s. For each flow rate, the power input was increased from zero to the maximum output that the wirebond could tolerate. For each test run, the temperature and pressure drop were closely monitored. After about 5 minutes steady state condition was identified and data was sampled continuously for about one minute. Using the calibration curve all temperatures were calibrated. After each test flow measurement was performed by collecting and weighing the DI water for certain amount of time. The power dissipation is determined from the product of the voltage and current measured at the heater.

It should be mentioned that actual heat input may be less than measured value due to the losses to the environment. It is found that power input measured agreed within 3% of the heat transferred to the water.

5.5 Experimental Results

5.5.1 First Sample

The first sample tested in the test loop was the channel with 67 μm hydraulic diameters, 400 μm length and aspect ration of 5. Fin thickness and channel width are 40 μm . The manifold had 120 μm inlet width, 240 μm outlet width and 13 inlet and outlet flow passes, and the depth of the manifold flow passes was 500 μm . The result of the pressure drop versus flow rate in this sample is presented in Figure 40. As seen pressure drop increases with increase in flow rate, and for the flow rate between 0.6 g/s and 1.2 g/s, pressure drop was between 5.8 kPa and 20.1 kPa. The main uncertainty of the measurement is for flow rate with 0.05 g/s error. The pressure drop uncertainty in the measurement was 0.02 kPa which is negligible.

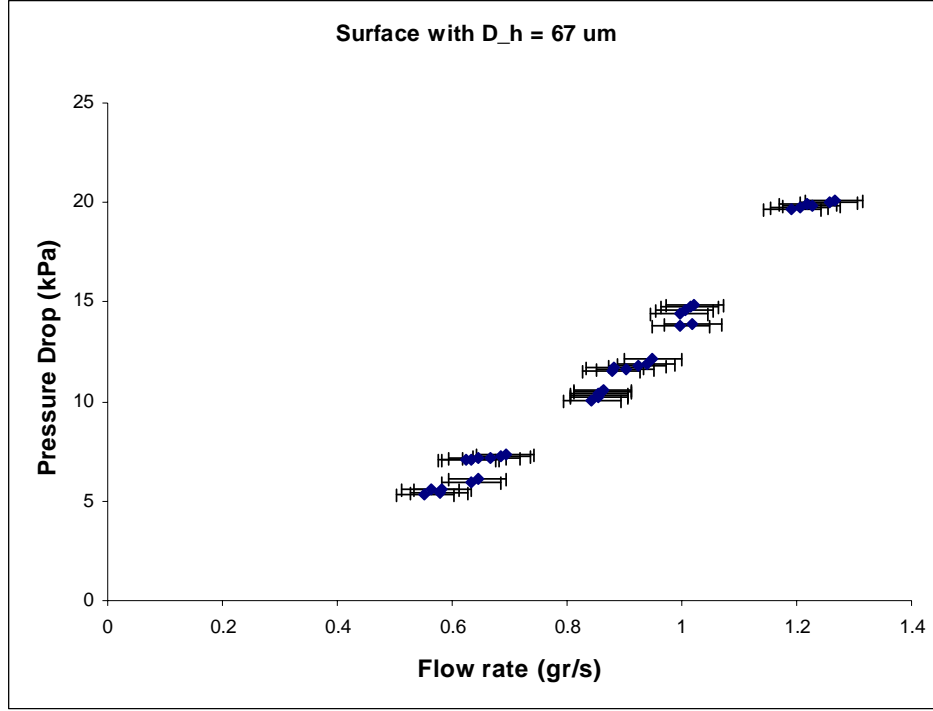


Figure 40: Variation of pressure drop versus flow rate for first sample with 67 μ m hydraulic diameter.

The heat transfer coefficient obtained at each flow rate is presented in Figure 41. The overall heat transfer coefficient h is calculated by

$$h = \frac{Q}{A\Delta T_m} = \frac{C_p \dot{m}(T_{out} - T_{in})}{A[T_w - 0.5(T_{in} - T_{out})]}$$

Heat transfer area A is defined as the total projected area. The heating power Q received by water is calculated by the energy conservation equation from the inlet and outlet working fluid temperature assuming negligible heat losses to the surroundings. As it is mentioned earlier heat losses to the surrounding was less than 3% of the total input heat. ΔT_m is the mean temperature difference between the channel walls and the working fluid. T_w is the average heater surface temperature and was determined by the three thermocouples placed on the heater. T_{in} and T_{out} are the inlet and outlet bulk

temperature of the working fluid. The mean temperature of the water $0.5(T_{in} + T_{out})$ is used to characterize the physical properties of the working fluid, including thermal conductivity K , density ρ , and specific heat C_p .

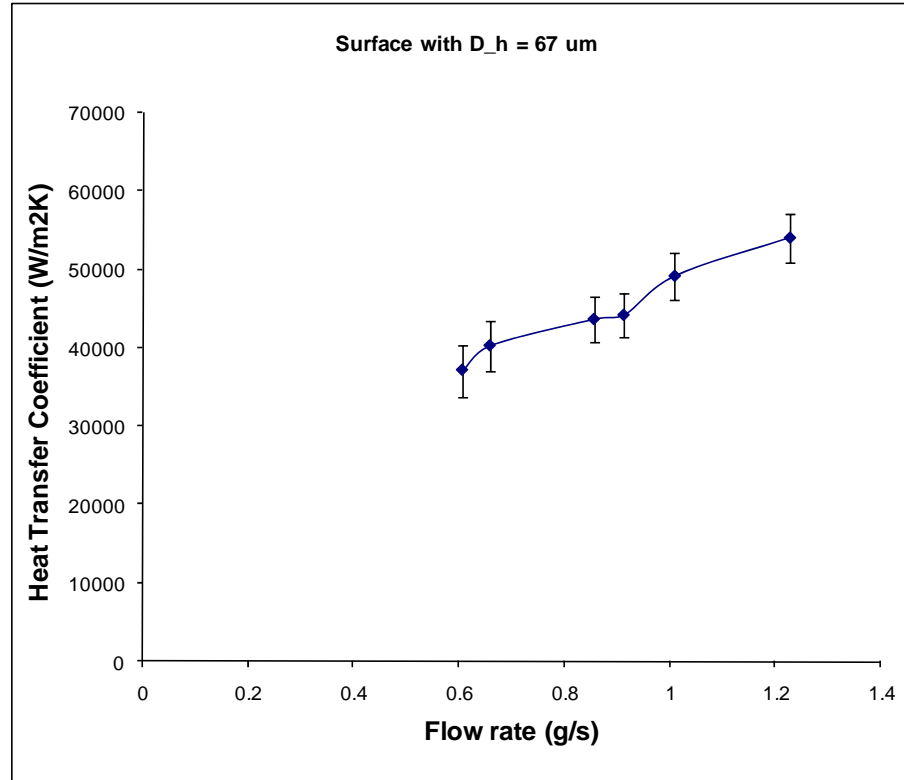


Figure 41: Variation of heat transfer coefficient versus flow rate for sample with 67μm hydraulic diameter.

As seen, the heat transfer coefficient increases as the water flow rate increases and at its peak, the heat transfer coefficient is 57528 W/m²K. The uncertainty in heat transfer coefficient for all test points averaged 7% with a maximum uncertainty of 8.9%.

Temperature difference in the water between the inlet flow and outlet flow versus input power at different flow rates is plotted in Figure 42. The maximum power

applied to this sample is 58 W, and water inlet temperature is 25 °C. As predicted, at each input power when the water flow rate was low, temperature difference was high and lower temperature difference occurs at higher flow rate. Also at constant flow rate by increasing input power, water temperature difference increase since the water heated up. The maximum water temperature difference between outlet flow and inlet flow occurred at maximum input power of 58 W and minimum flow rate of 0.66 g/s and was 20.3 °C.

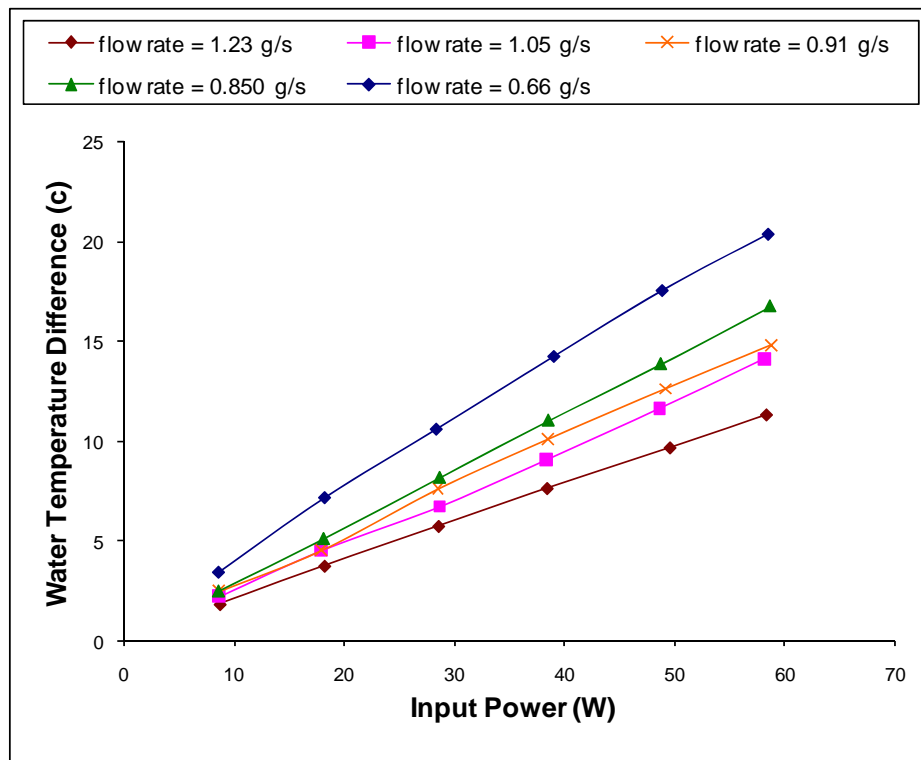


Figure 42: Variation of water temperature difference versus input power for sample with 67 μ m hydraulic diameter.

The variation of average surface temperature minus inlet water temperature, versus input power at different flow rate is presented in Figure 43. Here it is seen that surface temperature increases with increase in input power; however, it decreases with increase in flow rate due to higher heat transfer coefficient. The maximum

average surface temperature was 48.2 °C, attained at maximum input power of 58 W and minimum flow rate of 0.66 g/s.

By comparing Figure 42 and Figure 43 one can conclude that this heat sink can provide water at minimum temperature of 75 °C, and keep the average surface temperature bellow 110 °C for the solar cell application.

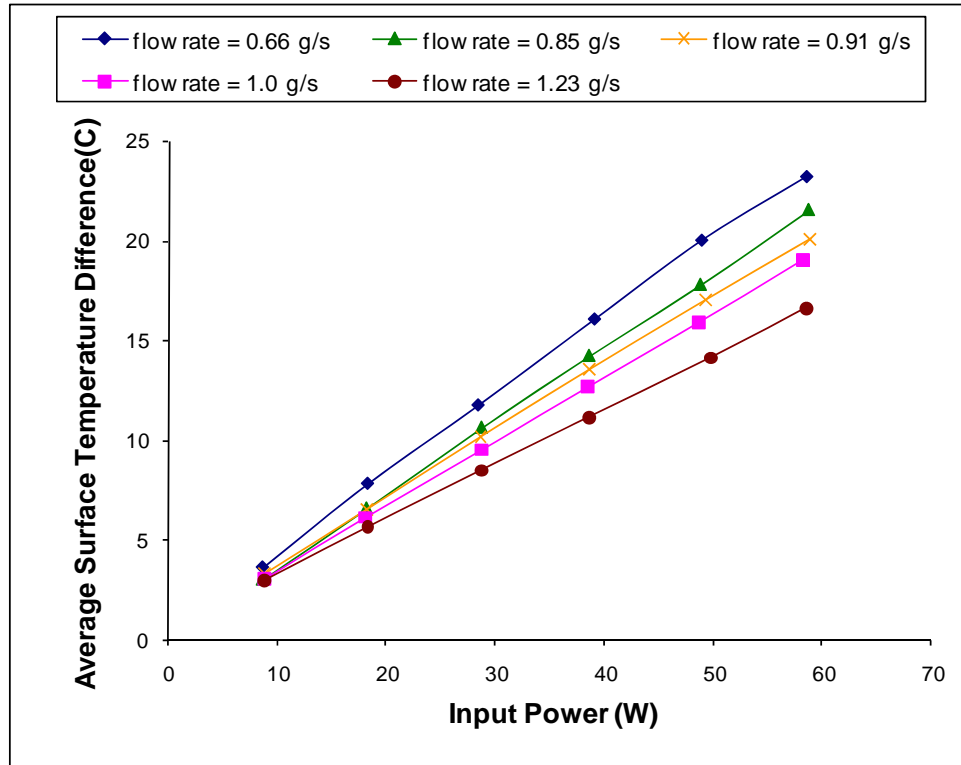


Figure 43: Variation of heater surface temperature difference versus input power for sample with 67μm hydraulic diameter.

5.5.2 Second sample

The second sample tested in the test loop had channel with 36 μm hydraulic diameter, 400 μm length, aspect ratio of 10 and fin thickness equal to channel width of 20 μm.

The manifold in this test had 120 μm inlet and 240 μm outlet width. The depth of the manifold flow passages was 500 μm and it had 13 inlet and outlet flow passages. In

Figure 44 the pressure drop versus flow rate is presented for flow rate between 0.3 g/s

and 1.2 g/s. Pressure drop was obtained between 3.6 kPa and 22.6 kPa. In this test case same behavior as of first test sample for pressure drop versus flow rate is seen. The major source of uncertainty is in flow rate measurement with the value of 0.05 g/s.

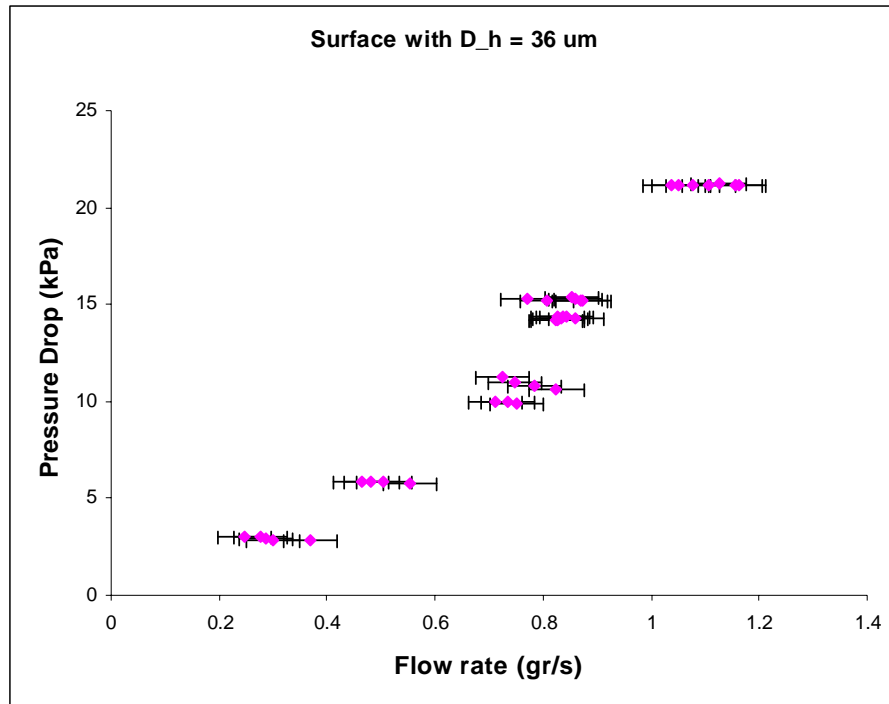


Figure 44: Variation of pressure drop versus flow rate for sample with 36 μm hydraulic diameter.

Heat transfer coefficient versus flow rate for this sample is presented in Figure 45. Similar to the first sample, the heat transfer coefficient is calculated and as seen it increased with flow rate. The uncertainty in heat transfer coefficient for all test points averaged 8.5% with a maximum uncertainty of 17%. Major source of uncertainty in these tests was also associated with measurement of flow rate.

As for the first sample, temperature difference between inlet water and outlet water temperature, versus input power at different flow rate is plotted in Figure 46. The

power increment in this sample was the same as the first, but the maximum power was increased to about 75 W and the inlet water temperature was 25 °C. The same trends was obtained for this sample, and at very low flow rate of 0.5 g/s the temperature difference in water increased to 30.3 °C at maximum input power of 75 W.

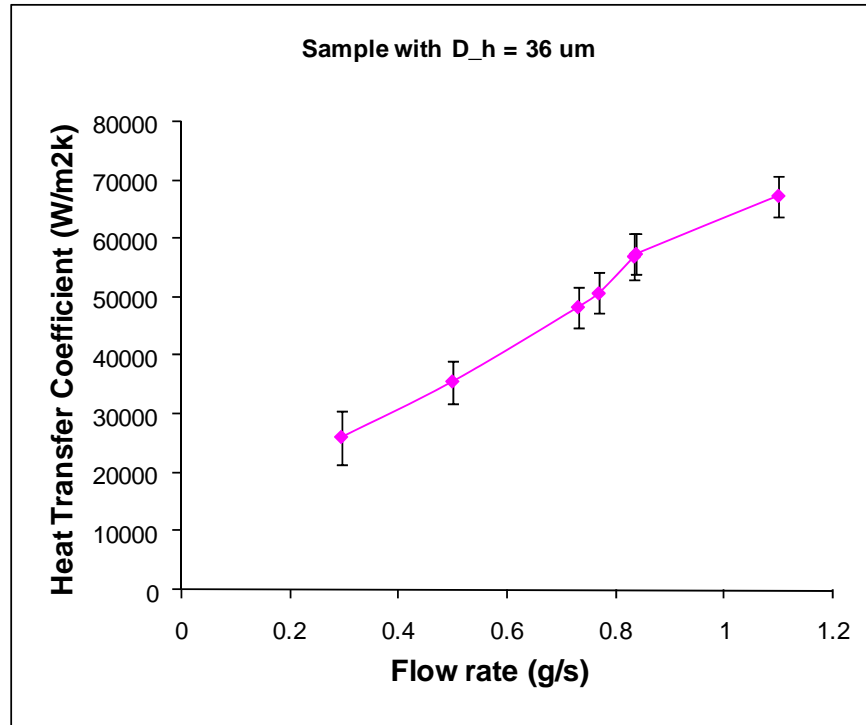


Figure 45: Variation of heat transfer coefficient versus flow rate for sample with 36 μm hydraulic diameter.

In Figure 47 the average surface temperature minus inlet water temperature, versus input power at different flow rate is presented. Same as the previous graph, the trend in this result are the same and for low flow rate of 0.5 g/s surface temperature increase to 58.4 °C at maximum input power of 75 W. When the flow rate increase heat transfer coefficient is higher therefore the surface is cooled better and has lower average temperature. These two graphs show that this heat sink can also provide hot

water at minimum temperature of 70 °C and keep the average surface temperature below 110 °C for solar cell application.

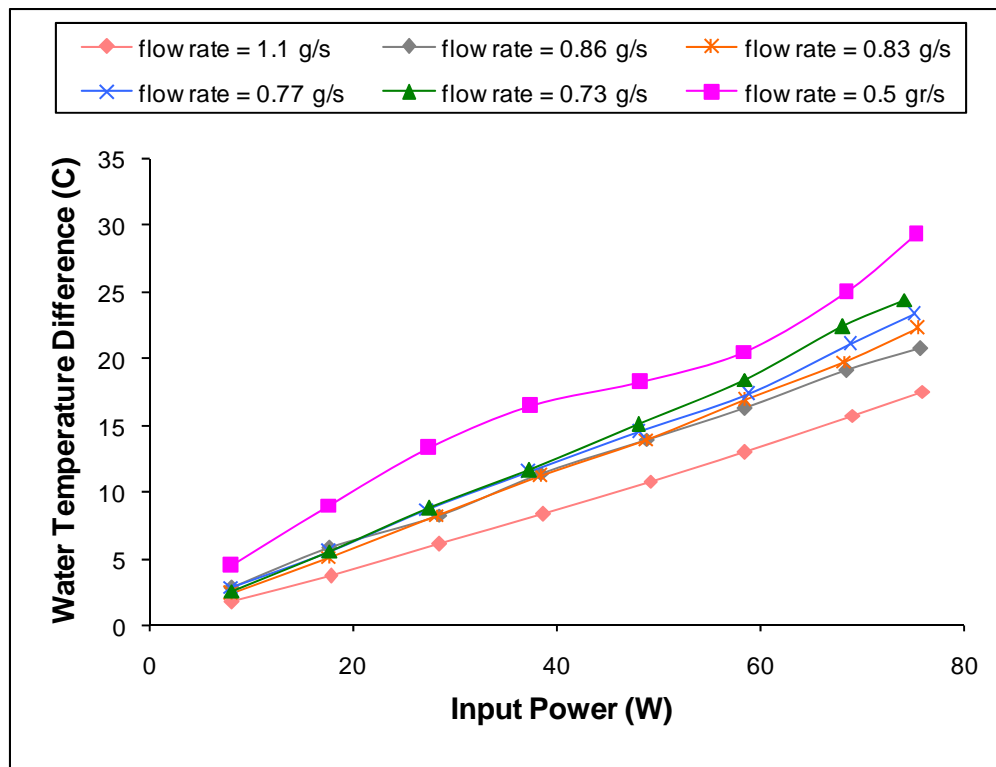


Figure 46: Variation of water temperature difference versus input power for sample with 36 μm hydraulic diameter.

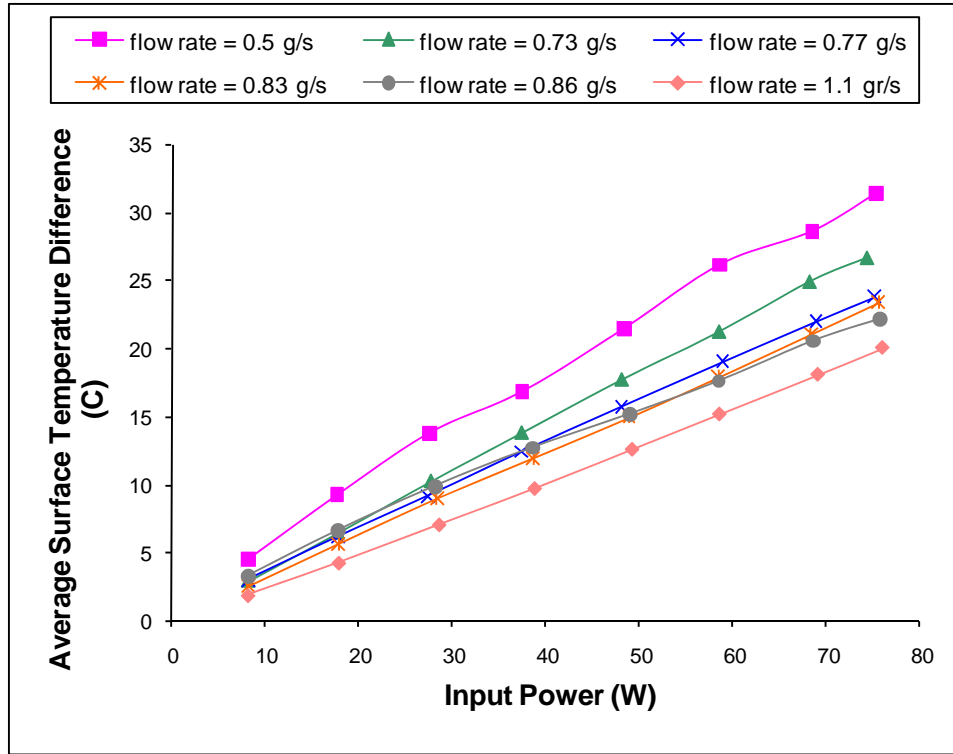


Figure 47: Variation of heater surface temperature difference versus input power for second sample.

5.6 Comparison Between the Results of the First and Second Sample

A comparison between the first sample and second sample pressure drop versus flow rate is presented in Figure 48. As seen in this figure, these samples follow the same trend in pressure drop and sample with 36 μm hydraulic diameter has slightly higher pressure drop due to smaller diameter resulting in an increase in the number of channels per centimeter, which consequently increases the pressure drop. In both cases flow distributor guide flow through the channels and divides flow into smaller channel length therefore the channel length is smaller and pressure drop is lower in compare with conventional micorchannels with one inlet flow and one outlet flow. It is known that due to higher flow velocity in the manifold the dominant pressure drop

occurs in the manifold and smaller fraction of the pressure drop occurs in the microchannel.

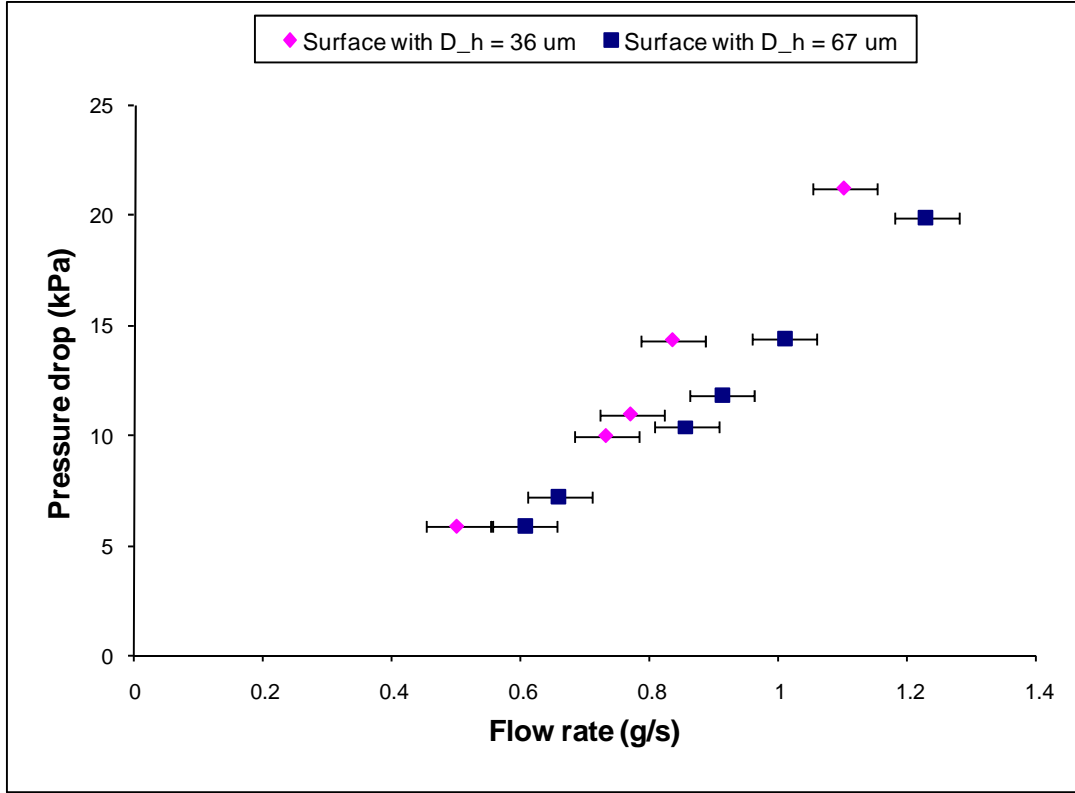


Figure 48: Comparison of pressure drop between first and second sample.

To calculate the pressure drop in the microchannel the following correlation by Jiang et al. [26] for friction factor in rectangular microchannel is used. The friction factor is correlated with Re for laminar flow condition with Reynolds number smaller than 600.

$$f = 1639 / \text{Re}^{1.48}$$

Pressure drop in the microchannels is calculated with following equation:

$$\Delta p = f \frac{L}{D_h} \times \frac{V^2}{2} \times \rho$$

where Δp is pressure drop across the microchannel, ρ is the water density in terms of the mean value of the inlet and outlet temperature, D_h and L are the hydraulic diameter and the length of microchannel, v is the average velocity of water and f is the friction factor.

Microchannel pressure drop is calculated for two test cases and subtracted from the overall pressure drop to find the manifold pressure drop as presented in

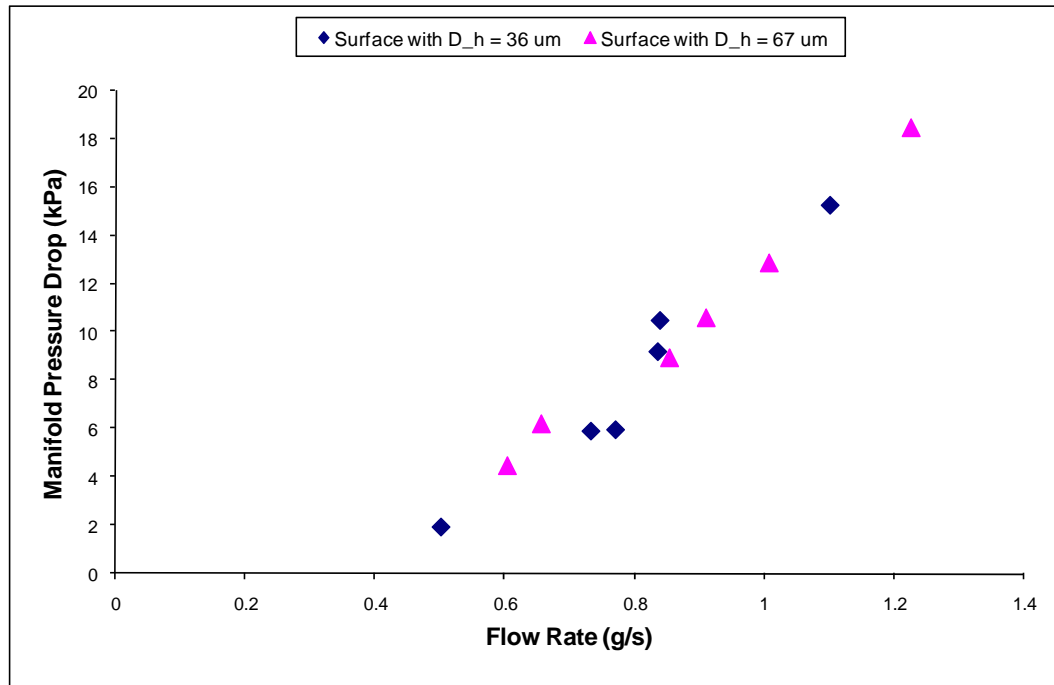


Figure 49.

Total pressure drop consists of two term, microchannel pressure drop and manifold pressure drop. As expected since both samples have manifold with same geometrical dimension to distribute the flow into the microchannels, pressure drop in their manifold has same value and as predicted this is the dominant term in the total pressure drop.

In Figure 50, for the test case with 67 μm hydraulic diameter two pressure drop terms are presented. On average microchannel pressure drop is 13% of the total pressure drop and as the flow rate increase contribution of microchannel pressure drop to total pressure drop decrease.

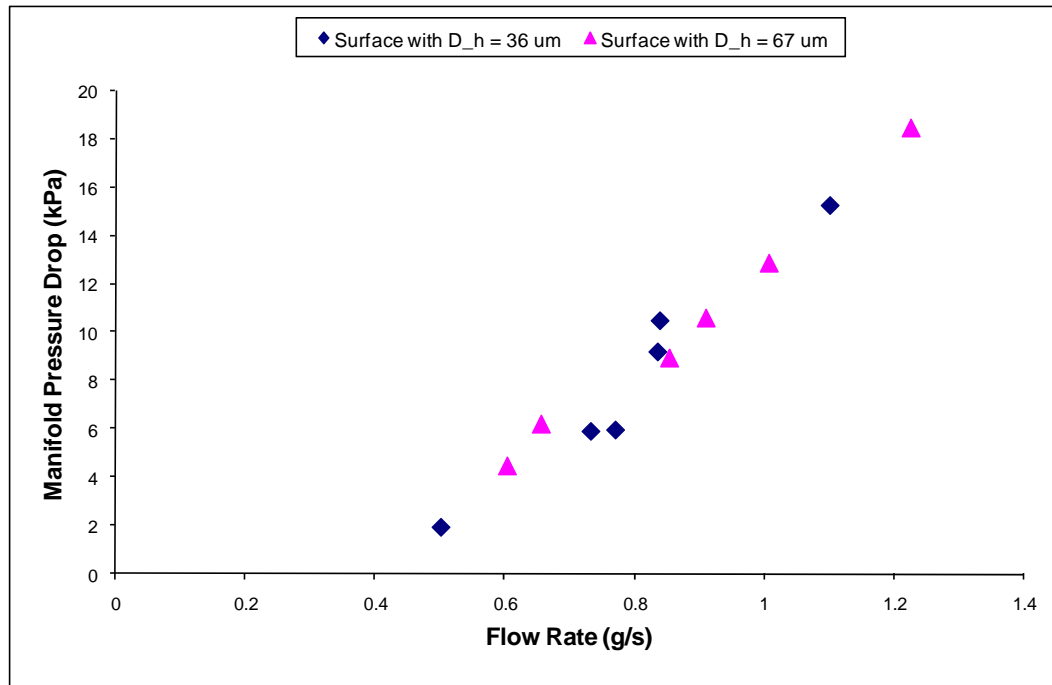


Figure 49: Pressure drop in the manifold for the two test cases.

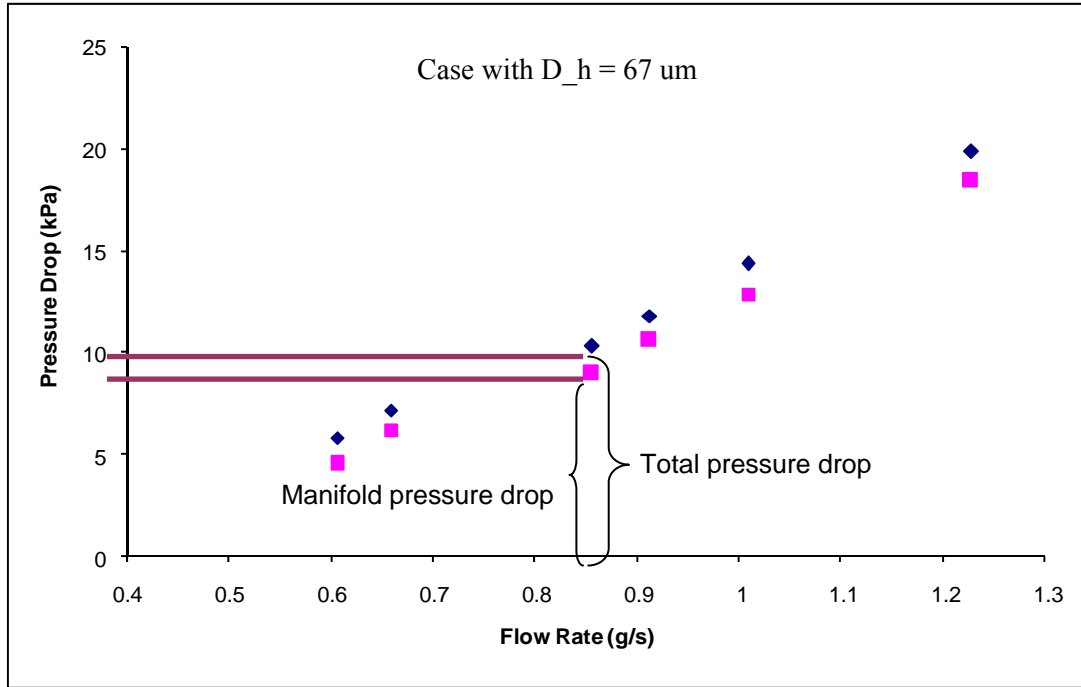


Figure 50: Total and manifold pressure drop for sample with hydraulic diameter of 67 μm .

Same calculation for case with 36 μm hydraulic diameter shows that the contribution of microchannel pressure drop in total pressure drop on average is 35%, which is higher in compare with previous case and the main reason is smaller hydraulic diameter and therefore this case higher total pressure drop. As the flow rate increase the ratio of microchannel pressure drop to total pressure drop decrease (Figure 51).

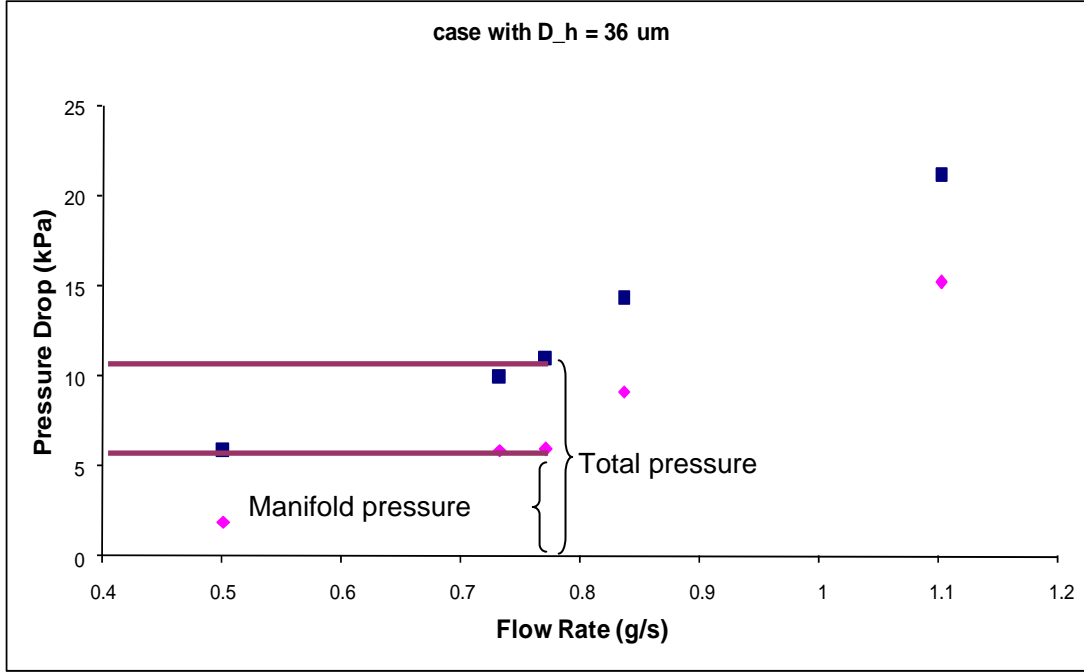


Figure 51: Total and manifold pressure drop for sample with hydraulic diameter of 36 μm .

Another comparison was done between Nusselt number versus Reynolds number for the two test samples. The overall Nusselt number for the de-ionized water flowing through the sample is defined as

$$Nu = \frac{hD_h}{K}$$

The mean temperature of the water is used to characterize physical properties of the de-ionized water and the hydraulic diameter is defined as $\frac{4A}{P}$. Figure 52 shows the effect of Reynolds number on the average Nusselt number. As the Reynolds number increases, a higher Nusselt number is obtained and overall agreement between these two samples is achieved. Since these two samples tested approximately at similar flow rate and the hydraulic diameter of the second sample is approximately half of first one the Reynolds number for second sample is half of the first sample.

These results were compared against the available literature, for which a study by Jiang et al. [26] was selected. Their research demonstrated that the average Nusselt number decreases from 12.9 to 3.0 with an increase in X^+ for rectangular microchannel (where X^+ is defined as $L/(RePrD)$). They observed two-flow regime depending on value of X^+ number. For the $X^+ < 0.05$, the average Nusselt number decreases sharply with increasing X^+ , whereas for $X^+ > 0.05$ the average Nusselt number decreases slowly with increasing X^+ . They proposed a Nu and X^+ correlation as:

$$Nu = 0.52 \left(\frac{Re Pr D_h}{L} \right)^{0.62}$$

Where Nu number increase with Re number in the entry region of thermal boundary layer in a microchannel and this effect enhance the heat transfer.

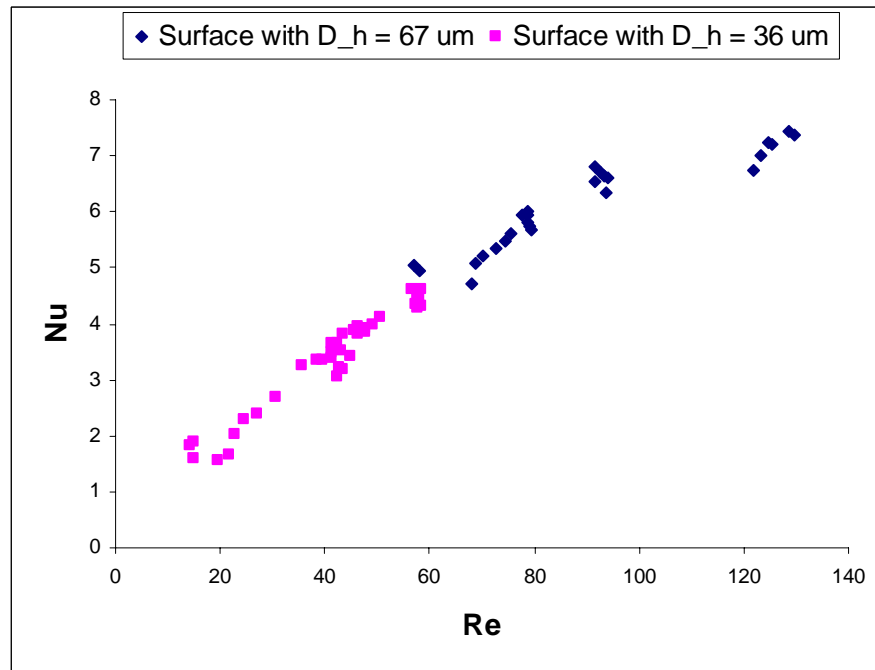


Figure 52: Variation of Nusselt number versus Reynolds number for first and second sample.

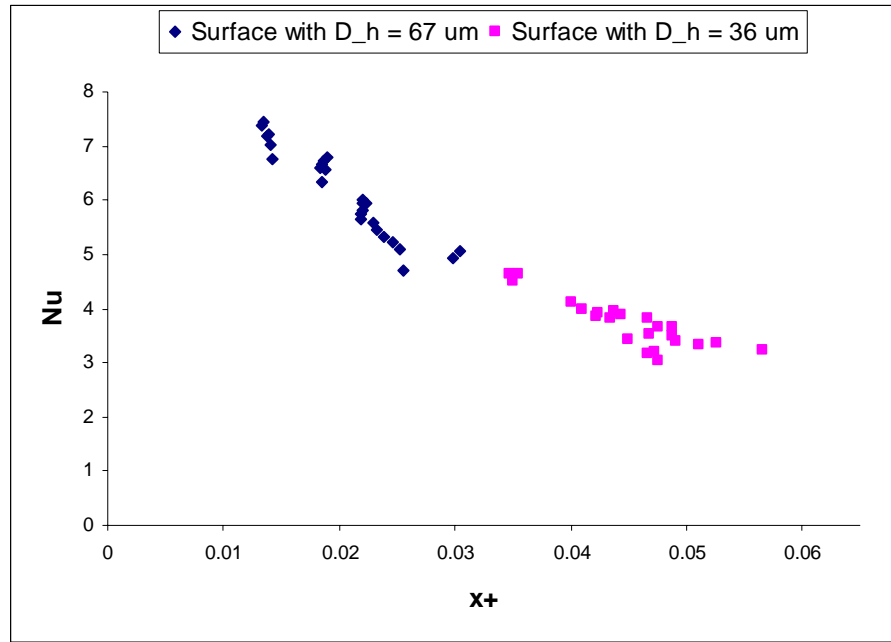


Figure 53: Variation of Nusselt versus X^+ for two sample cooler.

This trend is also observed in the results of this research. As presented in Figure 53, the average Nusselt number versus X^+ demonstrates a decreasing trend up to $X^+ = 0.05$, which proves that the flow should be in the developing regime. As discussed in Chapter 2, the manifold helps to promote redeveloping flow in each channel, which enhances the heat transfer capability.

Experimental results against Jiang et al. correlation are presented in Figure 54 and demonstrate reasonable agreement with the correlation. The effect of entrance region effect on heat transfer enhancement is the main goal of using flow distributor.

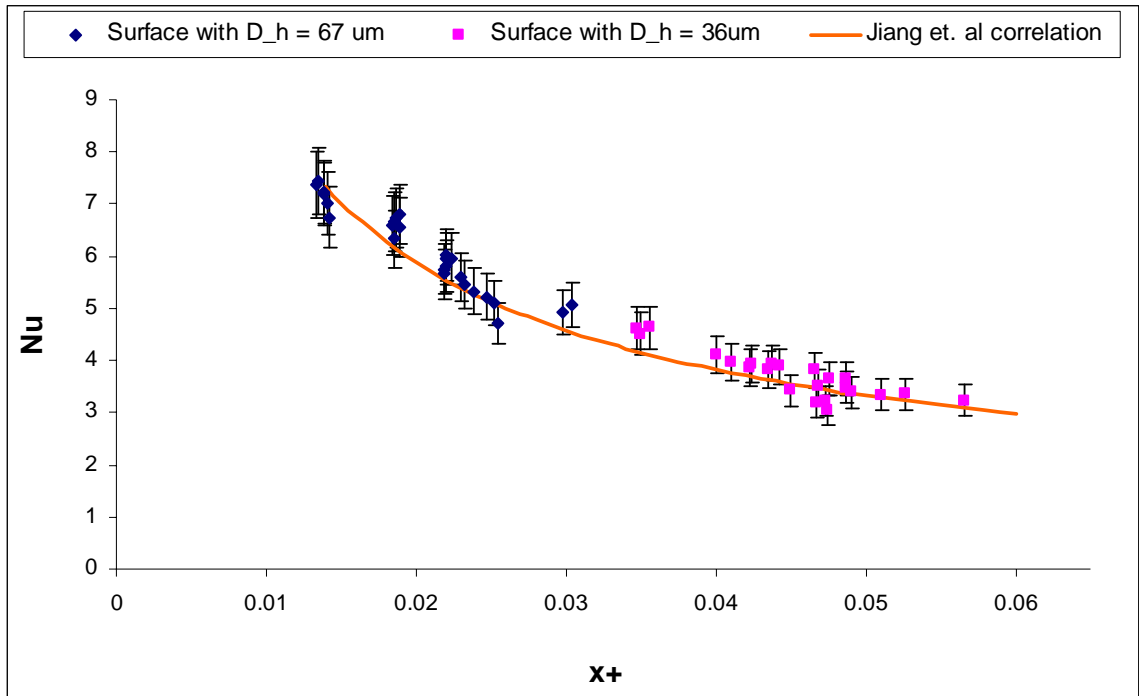


Figure 54: Comparison of Nusselt number versus X^+ number of the experiment against Jiang et al. [26] correlation.

5.7 Summary

As discussed in Chapter 2, this research is conducted to make a device capable of cooling the concentrated solar cells. The preliminary results of the tests on these two heat sinks demonstrated that manifold microchannel, microfabricated on silicon wafer can keep the average surface temperature below the limit for solar cell application and provide hot water for thermal application. Furthermore Manifold enhance the heat transfer by causing the flow to be in thermal entry region, but this technology needs more research to extensively examine the different aspects of it.

Chapter 6: Conclusions and Recommendations for Future Work

6.1 Introduction

The advantages and limitations of concentrated solar cells technology was characterized in this study. Realizing the limitation of the existing technology, development of manifold microchannel technology was proposed to overcome the problem. A manifold microchannel was fabricated using a micro fabrication technique. Experiments were conducted to study the performance of the cooling device and heat transfer coefficient and pressure drop of the device. This chapter summarizes the results and conclusions of this study and provides a number of recommendations to continue this investigation for future.

A literature survey on the advantageous and limitations of the concentrated solar cell technology and manifold microchannel were given in chapter two. The design requirements for the cooling device are identified and on that basis the cooling device's design was given in chapter three. Later in details the microfabrication procedure for the cooling device fabrication was given in chapter four. An experimental setup is designed for the device and difference performance parameters are measured in chapter five.

6.2 Conclusions

This work presented the results of research on an innovative manifold microchannel cooling system for performance improvement of concentrated solar cells. The

experimental tests have demonstrated that this cooling device can remove heat fluxes at high heat transfer coefficient. The maximum heat flux of 75 W/cm^2 tested in this research is correspond to 1000 sun concentration with simplifying assumption of 25% solar cell efficiency for maximum cell temperature at 2 pm and sun irradiance of 1000 W/m^2 for the condition where there is no convection or conduction from the bottom and top surfaces. The maximum heat transfer coefficient obtained in this research is $67470 \text{ W/m}^2\text{K}$ for flow rate of 1.1 g/s on test case with hydraulic diameter of $36 \text{ }\mu\text{m}$, aspect ratio of 10 and channel width equal fin width equal to $20 \text{ }\mu\text{m}$. High heat transfer coefficient obtained is due to redevelopment of the thermal boundary layer at each channel which is a consequence of using flow distributor (manifold). Since the flow is in thermal entry region Nusselt number is not constant and it is shown that Nusselt number is correlated with Reynolds number to the power of 0.62 and the experimental results are consistent with Jiang's et al. [26] correlation for Nusselt number versus Reynolds number for rectangular microchannel in thermal entry region condition. Low pressure drops recorded during the experiments correspond to low pumping power requirements for the cooling system. These two main characteristics of this cooling device make this technology highly promising for cooling of concentrated solar cells which, as discussed in chapter one, needs active and uniform cooling for substantial performance improvement, thus better commercial viability.

The fabricated cooling device demonstrated the development of a manifold microchannel device out of silicon, which confirms that manifold microchannel

technology that fabricated out of silicon could be used for solar cell cooling. The developed device is capable of dissipating large heat load, while maintaining the surface temperature below the limited temperature. Both test samples demonstrate that they can keep the average surface temperature below 110°C (maximum operating temperature for solar cell application) while they can provide hot water at minimum 70°C for thermal applications. Another important factor is that by fabricating this device out of silicon thermal resistance between the heated solar cell and the microchannel surface will be minimized. Equally important, in this device all the required components exist and makes it possible for the device being packaged in small size which makes it possible to introduce high concentrator mirror, yet small size solar cell technology. However it should be mentioned that although manifold could enhance the heat transfer coefficient by causing the redevelopment of thermal boundary layer but it causes larger pressure drop in the manifold in compare with the microchannel and this is the draw back of this system. Other fabrication technique and material could be used to overcome this problem.

It is shown that for test case with hydraulic diameter of $36\text{ }\mu\text{m}$ average 37% of total pressure drop occur in the microchannel while for sample with hydraulic diameter of $67\text{ }\mu\text{m}$ average 13% of the total pressure drop occur in the microchannel and the remaining occur in the manifold. These results demonstrate that to have high heat transfer coefficient and low pressure drop optimization on the microchannel and manifold geometrical dimension should be done.

The results of this research open an important path for utilization of solar energy in combined system to produce electrical energy and use the waste heat. Moreover it makes an important addition to the understanding of the manifold microchannel process.

6.3 Recommendations for Future Work

The experimental work conducted in this research simulated the heat flux of the solar cell with gold resistance heaters. One important direction in continuation of this research in the future is to fabricate the microchannel on the backside of an actual solar cell and make the cooler with actual test condition, to conduct experiments on the performance of this system and evaluate the performance of the proposed cooling device on an actual test section.

In another direction research can be done to make non uniform spacing manifold microchannel to cool non-uniformly distributed temperatures on surface. One of the main applications of this device would be in concentrated solar cell where due to a possible tracking system error or the concentrating system error, there may be non uniform temperature distributions on the heated surfaces; and this is another main issue in use of solar cells and another barrier in bringing this technology to the market place.

At the system level more tests should be done to understand the flow pattern under different operating conditions and optimize the dimension of the system, mainly the

manifold to increase the performance of the system while decreasing the manifold pressure drops.

6.4 Summary

It is clear that lots of opportunity exists for further research in this field. The manifold microchannel technology used in this research is an exciting field with strong relevance to solar cell applications. While the author believes that present work makes valuable contrition to the development of technology, there is no doubt that further research in this field absolutely needed to expand implementation of concentrated solar cell technology into the market place.

Bibliography

1. R. M. Swanson,” The promise of concentrators” Prog. Photvolt. Res. Appl., 8 (2000) 93-111.
2. D. Cooke, P. Gleckman, H. Krebs, J. O’Gallagher, D. Saige, R. Winston,” Sunlight brighter than sun”, J. Nature, 346 (1990) 802.
3. A. Williams, “The Handbook of Photovoltaic Application”, The Fairmont Press Inc., 1986.
4. A. Luque, G. Sala, J. C. Arboiro,” Electric and thermal model for non-uniformly illuminated concentration cells”, J. Solar Energy Materials and Solar Cells, 51 (1998) 269-290.
5. J. I. Rosell, X. Vallverdu, M. A. Lechon, M. Ibanez, “Design and simulation of a low concentrating photovoltaic/thermal system”, J. Energy Conversion and Management, 46 (2005) 3034-3046.
6. J. S. Coventry,” Simulation of a concentrating PV/ Thermal collector using TRANSYS, ANZSES Solar Energy Conference, Newcastle, Australia, 2002.
7. J. S. Coventry, E. Franklin, A. Blakers,” Thermal and electrical performance of a concentrating PV/thermal collectors: results from the ANU CHAPS collector“, ANZSES Solar Energy Conference, Newcastle 2002.
8. A. Fahrenbruch, R. Bube,” Fundamentals of solar cells”, Academic Press, New York, 1983.
9. T. Markvart, “Solar electricity”, 2nd ed. Wiley, New York, 2000.

10. J. S. Coventry," Performance of a concentrating photovoltaic/ thermal solar collector", J. Solar Energy, 78 (2005) 221-222.
11. D. Meneses-Rodriguez, P. P Horley, J. Gonzalez-Hernandez, Y. V. Vorobiev, P. N. Gorley," Photovoltaic solar cells performance at elevated temperatures", J. Solar Energy, 78 (2005) 243-250.
12. I. Anton, G. Sala, D. Pachon," Correction of the V_{oc} Vs. temperature dependence under non-uniform concentrated illumination", 17th PVSEC (2001)
13. I. Anton, R. Solar, G. Sala, D. Pachon, " IV testing of concentration modules and cells with non-uniform light patterns".
14. M. Brogren, P. Nostel, B. Karlsson," Optical efficiency of a PV-thermal hybrid CPC module for high latitudes" J. Solar Energy 69 (2001) 173-185.
15. H. P. Garg, R. S. Adhikari," Performance analysis of a hybrid photovoltaic/ thermal collector with integrated CPC troughs" Int. J. Energy Res. 23 (1999) 1295- 1304.
16. G.N. Tiwari, Solar Energy Technology Advances, 2006.
17. G. Sala, J. C. Arboiro, A. Luque, L. C. Zamorano, J. C. Minano, C. Dramsche," The EUCLIDES prototype, an efficient parabolic trough for PV concentration", in Proc 25th Photovoltaic Specialists Conf., IEEE, New York, 1996, pp. 1207-1210.
18. D. b. Tuckerman, R. F. W. Pease," High performance heat sink for VLSI", IEEE Electron. Device Lett. EDL2 (1982) 126-129.
19. G. M. Harpole, J. E. Eninger," Micro-channel heat exchanger optimization", Seventh IEEE Semi-Therm Symposium

20. D. Copeland, M. Behnia, W. Nakayama, "Manifold microchannel heat sink: Isothermal analysis", IEEE Transaction on Component, Packaging, and Manufacturing Technology-Part A, Vol. 20 No. 2 (1997) 96-102.
21. J. H. Ryu, D. H. Choi, S. J. Kim, "Three-dimensional numerical optimization of manifold microchannel heat sink", International Journal of Heat and Mass Transfer 46 (2003) 1553-1562.
22. J. L. Xu, Y. H. Gan, D. C. Zhang, X. H. Li, "Microscale heat transfer enhancement using thermal boundary layer redeveloping concept ", International Journal of Heat and Mass Transfer 48 (2005) 1662-1674.
23. Y. Wang, G-F. Ding," Experimental investigation of heat transfer performance for a novel microchannel heat sink", Journal of Micromech. Microeng 18 (2008) 035021.
24. Y. Wang, G-F. Ding, S. Fu, "Highly efficient manifold microchannel heat sink", Electronic Letters Vol. 43 No. 18.
25. L. Everhart, N. Jankowski, B. Geil, A. Bayba, D. Ibitayo, P. McClusky," Manifold microchannel cooler for direct backside liquid cooling of SiC power device", Proceeding of the fifth International Conference on Nanochannels, Microchannels and Minichannels ICNMM2007.
26. P. X. Jiang, M. H. fan, G. S. Si, Z. P. Ren, "Thermal-Hydraulic performance of small scale micro-channel and porous-media heat-exchangers", International Journal of Heat and Mass Transfer 44 (2001) 1039-1051.
27. M. J. Madou," Fundamentals of microfabrication", Second edition.

28. K. r. Williams, K. Gupta, M. Wasilik, "Etch rates for micromachining processing",
Journal of Microelectromechanical System, Vol. 12 No. 6 December 2003.
29. X. Wei, Y. Joshi, M. Patterson, » Experimental and numerical study of stacked
microchannel heat sink for liquid cooling of microelectronic devices »,
Transaction of ASME, Vol. 129 October 2007.
30. R. F. Wolffenbuttel, "Low-temperature intermediate AU-Si wafer bonding;
Eutectic or silicide bond", Sensors and Actuators A, 62 (1997) 680-686.
31. R. F. Wolffenbuttel, K. D. Wise, "Low-temperature silicon wafer to wafer
bonding using gold t eutectic temperature", Sensors and Actuators A, 43 (1994)
223-229.
32. M. Aslam, J. V. Hatfield, "Fabrication of thin film microheater for gas sensors on
polyimide membrane", IEEE, 2003.
33. [http://ap.pennnet.com/display_article/260447/36/ARTCL/none/none/1/Wire-
Bonding-Considerations/](http://ap.pennnet.com/display_article/260447/36/ARTCL/none/none/1/Wire-Bonding-Considerations/)
34. T. M. Baumer, Edvin Cetegen, Michael Ohadi, Serguei Dessiatoun, "Force-fed
evaporation and condensation utilizing advanced micro-structured surfaces and
micro-channel" Microelectronics Journal 39 (2008) 975-980.
35. B. C. Pak, W. C. Chun, B. J. Beak, D. Copeland, "Forced air cooling by using
manifold microchnnel heat sinks", Advanced Electronic Packaging 2 (1997)
1837-1842.
36. <http://www.strand7.com/>